

Multifractal Recalibration of Neural Networks for Medical Imaging Segmentation

Miguel L. Martins

Department of Computer Science, University of Porto & INESC-TEC
 miguel.l.martins@inesctec.pt

Miguel T. Coimbra

Department of Computer Science, University of Porto & INESC-TEC
 mcoimbra@fc.up.pt

Francesco Renna

Department of Computer Science, University of Porto & INESC-TEC
 francesco.renna@fc.up.pt

Abstract

Multifractal analysis has been pivotal to uncover the regularities of several self-seeding phenomena in various scientific measurements. However, although methods characterizing the so-called *multifractal spectrum* (MFS) received a considerable amount of attention in classical computer vision, its role in the era of modern deep learning has been relatively limited. In fact, some end-to-end approaches emerged, mainly for the task of texture recognition. These new methods rely on computationally heavy pooling operations, or aggressive decimation of the feature space in order to enable training and inference to be feasible in time, which are unsuitable for tasks such as semantic segmentation.

With this motivation, we set forth two new inductive priors that address these limitations – Monofractal and Multifractal Recalibration. We leverage the relationships between the probability mass of the exponents and their MFS to build a statistical description of each embedding of the encoder of the network. We thus formulate our solutions as channel-attention functions in the context of convolutional neural networks.

We build an experimental framework centered around the U-Net and show that Multifractal recalibration can lead to substantial improvements over a baseline augmented with other well-established channel attention functions that also describe each channel in terms of higher-order statistics. Due to the proven effectiveness of multifractal analysis in capturing pathological regularities, we conduct our experiments over three public datasets from diverse medical modalities: ISIC18 (dermoscopy), Kvasir-SEG (endoscopy), and BUSI (ultrasound).

An empirical analysis also reveals new insights into the dynamics of these attention layers. We find that excitation response does not get increasingly specialized with encoder depth in the U-Net due to its skip connections, and that its effectiveness may be linked to global statistics of their instance-variability.

Keywords. semantic segmentation, multifractal formalism, fractal geometry, medical imaging, deep learning, inductive prior

AMS subject classifications. 68Q25, 68R10, 68U05

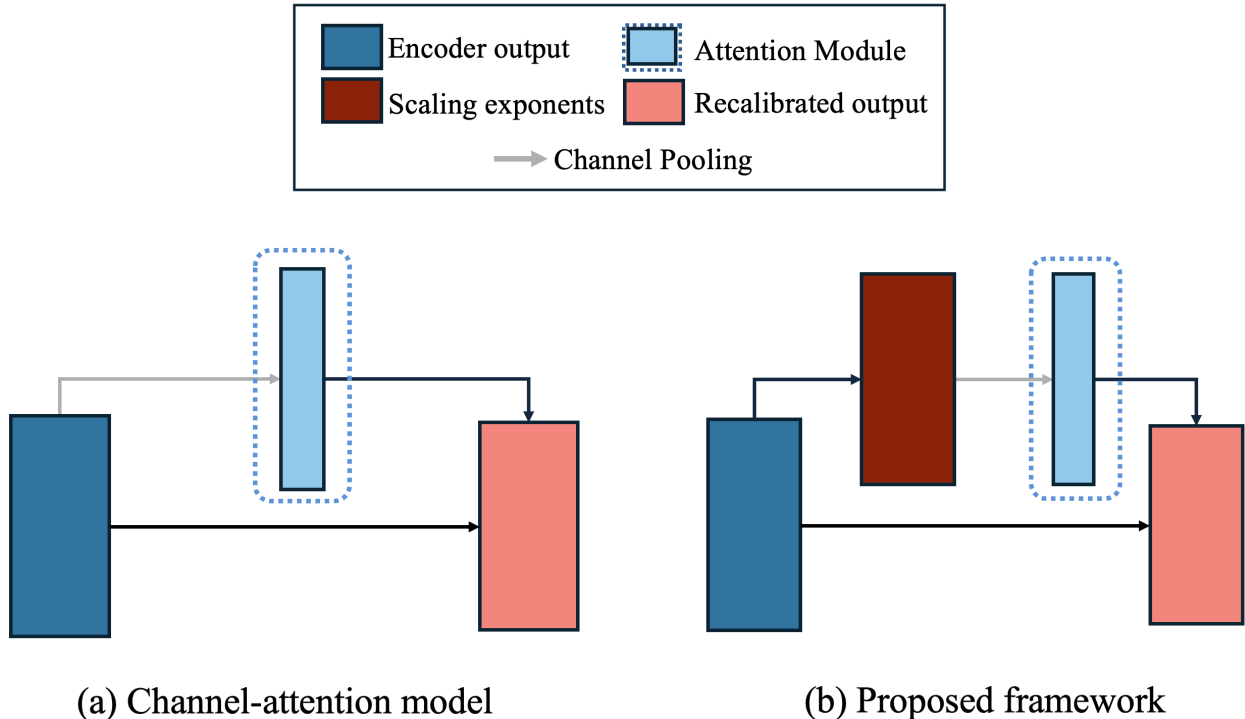


Figure 1: (a) The typical channel attention model where some statistics is pooled directly from the encoder output. (b) Our proposed approaches use statistics derived from the scaling exponents of the features maps.

1 Introduction

Pathological phenomena may be described as a *state* of a physiological system that evolves in a self-seeding, cascading fashion [33]. These states are observed as complex patterns in medical imaging modalities, whose regularities may be disentangled through the lens of *Fractal Geometry*, the field of mathematics centered around the study of mathematical structures that have fine-structure, i.e., detail at all scales [15]. This degree of scale-invariance may be captured in terms of a single (monofractal) or multiple (multifractal) scaling exponents that embody the *dimension* of the structure [14]. This *self-similarity* in distribution across scale is especially useful to describe textures as stationary stochastic processes [9, 69, 72, 11].

In Medical Imaging, both structural and surface-level regularities may be leveraged [33]. Examples range from histology [3, 46, 56], endoscopy [19, 49], dermoscopy [52, 8], to magnetic resonance imaging (MRI) [35, 28, 37] and many others (see [39, 33] and references therein). On the other hand, Fractal Geometry has received limited attention in the deep learning era, especially in the design of end-to-end architectures. This trend recently changed, and some successful approaches have been proposed for texture classification [72, 11, 10] and few-shot learning [76]. Bridging this gap for semantic segmentation is the main contribution of this paper, under the assumption that the inductive prior of a convolutional neural network (CNN) encoder carries information about the image’s scaling laws across its layers.

Grounded in multifractal analysis, we propose two new attention functions designed around the U-Net [57], the main specialist model alternative to current foundational approaches [26, 27, 42]. These functions describe cross-channel dynamics by deriving single or multiple statistics over the

local scaling exponents of each filter (see Figure 1). We show substantial improvements over several attention functions [58, 38, 53] in terms of segmentation performance in three public medical image segmentation datasets. During this investigation we also conduct an empirical analysis in an effort to shed some light on the reason behind the disparity of performance between different statistical channel functions. Our findings suggest that intuitions held by the community behind the mechanisms that govern these layers [22, 58, 51, 18] do not seem to hold in the case of semantic segmentation. Briefly, our experiments suggest that these functions do not seem to learn to “filter non-informative channels”. Inspection of their response dynamics are indeed antithetical to this assumption: a certain range of instance variability is actually desirable.

1.1 Contributions

Current end-to-end architectures [72, 11, 10] that leverage multifractal primitives (described in Section 2.3) are engineered for recognition, and most draw parallels with the underlying formalism in a very ad hoc fashion. We only identified the fractal encoder in [72] to be close to a true multifractal prior. Moreover, these methods rely on computationally expensive fusion approaches that require spatial or channel upsampling and/or downsampling [72, 76, 10], aggressive shape normalization across spatial and channel dimensions [11], and inefficient [10] or repeated computations [11] of extensions of the differential box counting (DBC) algorithm.

We address these issues by deriving statistics over the local scaling exponents with a theoretically guided rationale. This work has a special focus on the U-Net, but note that the methods set forth may be readily applied to any deep neural network (DNN) architecture. We then draw inspiration from statistical channel attention functions [22, 58, 38, 53, 18], but we recalibrate the output of the network as a function of the scaling exponents, instead of using the direct responses of each encoder block.

This paper also extends very preliminary empirical work where we presented an early version of Monofractal recalibration [43]. However, the experimental setup has been substantially upgraded with more extensive and rigorous statistical analyses, more datasets, better training and cross-validation routines, more baseline architectures [58, 38, 53] and ablation experiments, and a more detailed analysis of how these attention mechanisms behave. Finally, we propose an entire new attention module that displays superior performance in general: *Multifractal recalibration*. All of the introduced inductive priors are also studied from a principled perspective through the lens of multifractal analysis.

Our main contributions are summarized as follows¹:

1. An efficient end-to-end way to compute the local scaling exponents adequate for dense prediction tasks.
2. Two novel attention functions theoretically grounded in multifractal analysis.
3. An experimental analysis of other statistically informed recalibration strategies beyond squeeze-and-excitation (SE) [58], such as style based recalibration (SRM) [38] and frequency channel attention (FCA) [53] for the purposes of medical image segmentation.

1.2 Paper structure

The remainder of the paper is structured as follows. Section 2 provides a detailed description of the application of Fractal Geometry in Computer Vision, Medical Imaging, and with regards to

¹Our code is available at <https://github.com/miguelmartins/multifractal-recalibration/>.

its latest advancements in the deep learning era. In Section 3 we conduct a background review of the core concepts and set forth the formalism that will contribute to our proposed approaches, presented in Section 4. The performance of Monofractal and Multifractal recalibration is measured on three public datasets in Section 5, alongside an empirical analysis of the excitation responses. Finally, in Section 6, we identify limitations and future work, after highlighting our main theoretical and experimental findings.

2 Related Work

This section provides a review of the prior art, with initial context from classical computer vision, and then re-contextualized within more contemporary natural and medical imaging. Finally, we study how Fractal Geometry has been leveraged to develop novel inductive biases for deep learning methods.

2.1 Fractals in Classical Computer Vision

The first applications of Fractal Geometry in Computer Vision date to back the 1980s [5]. In this era, Pentland seminally argued that since the intensity of an image is a function of the angle between the illuminant and the surface normal, then if the normals follow a Fractal Brownian distribution and the perspective is kept constant, then the fractal dimension is carried to a digital photograph [50]. The introduction of the DBC algorithm [60] was pivotal to increase adoption of fractal geometry in the Computer Vision community, since it allowed for efficient estimation of the number of boxes covering a 3D surface (e.g., a gray-scale image).

The fractal dimension has been used extensively as a descriptor for texture [9, 71, 62]. Quantities related to the more general *set of generalized dimensions* [69] embedded within morphological models and clustering approaches were also demonstrated to be effective in the semantic segmentation of textural attributes, such as mosaics of textures from the Brodatz album [6]. Other classical approaches for multifractal segmentation can be found in the references of [69, 62].

In [63], Vehel et al. propose multifractal formalism as an alternative to the traditional theory of filtering. They noted that the differentiation operation commutes with convolution, and so edges and regions of interest were found after the image was smoothed through convolution with some function g . Thus, by leveraging Multifractal formalism, one could potentially assign each point to a specific primitive (e.g., an edge) depending on the scaling exponent around its (local) neighbourhood, and each resulting on a *level set partition* that could be associated with the output of the convolution of the image with said filter g .

Vehel et al. also introduced the important idea of capturing this scaling behaviour as a function of several different *capacity functions* (such as the maximum, minimum, sum, etc.) in order to mitigate the noise sensitivity these methods display in practice. This inspired several contributions, where quantities related either to a set of fractal dimensions [62], or even the so called multifractal spectrum (MFS) [14, 71], $f(\alpha)$, were computed for a set of general filters, each defining a *measure* of the original (gray-scale) image.

Most of these early approaches were tailored towards gray-scale images. Inspired by multifractal theory [5] Ivanovici et al. proposed to measure the Fractal Geometry of RGB images [29, 30], by extending the concepts of Box dimension to 5-dimensional metric spaces.

2.2 Fractals in Medical Imaging

Physiologic systems have been described as inherently (multi)fractal since they evolve in a self-seeding, cascading fashion [33]. In fact, the theory of fractal and self-organizing structures has been proposed as a fundamental design principle of life itself [36]. *Fractalomics* [40] has been proposed to leverage statistical quantities based in fractal geometry due to its effectiveness at describing quantitatively morphological cellular structure complexity of cellular and biological tissues. Pathologies such as tumors have also exhibited fractal properties in both space and time [45]. For example, in dermoscopy, the fractal dimension was used to associate the regularity of the boundary of dermatological lesions with their severity [52]. This was eventually extended to include lesion texture to enhance classification [8]. It has been used to segment calcifications or regress bounding boxes in lesions captured in breast ultrasounds [61, 73]. It was also adopted for MRI to segment or classify tumors [35, 28, 37]. Its power to derive texture features significantly contributed to the increase of classifier accuracy in several histopathology modalities [3, 46, 56] as well as polyp and mucosal characterization in endoscopy [19, 49].

In fact, fractal and multifractal methods intersect with virtually all medical modalities in such a profound way that a thorough review of the art would require its own publication, so we refer the interest reader to [39, 66]. In the case of medical images, although the number of use-cases is broad, the type of techniques is relatively narrow, and do not differ significantly from the rest of the computer vision literature.

2.3 Fractals in Modern Computer Vision

Fractal geometry has received minimal attention as a design component for end-to-end deep learning architectures until relatively recently. In fact, prior to this paper, we found no end-to-end architectures for semantic segmentation. One of the main limiting factors is the expensive (and often non-differentiable, in the case of DBC) multi-scale analysis required to compute the local scaling exponents. Moreover, it is not entirely clear how fractal geometry fits in architectures such as CNNs, since they can learn arbitrary functions, and are thus not constrained to behave strictly as a set of Wavelet basis functions, as typically required in multifractal formalism. In the context of contemporary medical imaging (multi)fractal techniques have only been leveraged for static feature extraction for the purposes of classification using pre-trained DNNs [44, 56, 70, 49].

Fully end-to-end approaches have only been recently developed in the computer vision community. For texture classification, Yong Xu et al. [72] adapted their hand-crafted approach [71] to be supported end-to-end. Their work was motivated to complement global average pooling (GAP) with relaxed soft version of the MFS. After computing a soft-histogram over Q level sets, they compute a quantity proportional to the fractal dimension by max-pooling operations of increasing size for each level set Q . They fuse the soft MFS with GAP using bilinear pooling. Chen et al. [11] assume that a CNN is roughly a counterpart to the wavelet transform and consider that the fractal dimension is encoded throughout the layers and channels of a CNN, i.e., it as a function of a four-dimensional tensor (height, width, channel, and layer). They relax the DBC algorithm [60] to be used during training of the CNN. The surface tensor is constructed by imposing size-normalization constraints over spatial and channel dimensions of each layer. The proposed DBC algorithm is computed in overlapping windows and they learn a set of soft histograms for each l . Like [72] they also use a GAP layer on the embedding, but instead of bilinear pooling, they simply concatenate both feature maps.

For the task of few-shot learning, [76] introduced the fractal dimension as a prior for intra (inter) class similarity (dissimilarity), under the pretense that image regularity will differ across semantic

categories. The DBC is also adapted, this time solely by removing the non-differentiable rounding functions. Since they assume a perfect linear relationship, they skip the ordinary least-squares (OLS) step required to estimate the scaling exponents [71] and collect the point-wise estimate of the DBC in order to eventually compute the so-called *fractal embedding*.

Recently, [10] proposed the Multi-layer Fractal Encoding Network (MFEN). The box-dimension is computed by exhaustive thresholding of the ℓ_2 -norm distance of all points. The fractal dimension of each layer is derived using the ridged regression method. These fractal features are concatenated with the per-layer global average pooling output and a final dense multilayer perceptron (MLP) outputs the final predictions.

2.4 Statistical Channel Attention Functions

Squeeze-and-Excitation Networks [22] (SE) had a profound impact in modern deep learning architectures. SE is a simple *plug in* component that allowed each encoder in a CNN to have global receptive field. This was made possible since the input at depth l is recalibrated according to some *channel attention function* g . In this case, g is the output of an MLP over the GAP of some encoder at depth $l - 1$. One of the main limitations of the original SE module is the fact that GAP is a very limited feature descriptor by virtue of (a) being a global descriptor, by (b) being the simplest statistic one can compute to describe each filter, and (c) by the representation power and compute requirements of g . The reader is referred to [18] where a very comprehensive survey of extensions to SE is presented.

In [16], the second-order statistics are modelled through the covariance matrix across channels. However, they had to reduce the total number of channels in layer l , C_l , by means of 1×1 convolution to mitigate the introduced computational burden. The authors of [38] propose the style-based recalibration (SRM) module that uses both global average and standard deviation pooling to expand the receptive field of f_l . They learn a non-linear map of the mean and variance of each channel using channel-wise dense layers. In [53], the frequency channel attention (FCA) module was introduced. The authors illustrated how GAP is proportional to the lowest frequency component of the 2-dimensional Discrete Cosine Transform (DCT).

Specifically to Medical Imaging Segmentation, [58] propose recalibration using two branches: the *channel squeeze spatial excite* branch (cSE), a direct implementation of the original SE module, and the *spatial squeeze channel excite* (sSE) branch, that acts as spatial attention [47]. The output layer is an element-wise max-out between these two branches (scSE). The pursuit of channel-wise descriptions was further explored in [51, 55], but explicitly tailored to 3D segmentation and without emphasis in points (a) and (b), but in terms of (c). Related to the latter, other approaches demand an increasing amount of compute and/or architectural changes, such as introducing Transformers [64, 23, 4].

3 Preliminaries

In the remainder of this work, we will denote the input of a DNN encoder, Ψ , with an input tensor $\mathbf{X} \in \mathbb{I}_0$, so that $\Psi_l(\mathbf{X}) = \Psi_l \circ \dots \circ \Psi_2 \circ \Psi_1(\mathbf{X})$ where $\Psi_l : \mathbb{I}_{l-1} \rightarrow \mathbb{I}_l$ for $\mathbb{I}_l \equiv \mathbb{R}^{H_l \times W_l \times C_l}$. Thus, $l \in \{1, \dots, L\}$ indexes the layers of Ψ . Furthermore, $\Psi_{lhw c}$ signifies the c -th channel, at position (h, w) of the l -th layer. Assume henceforth that this indexing is consistent throughout and that index omission implies tensor slicing, e.g. $\Psi_{lc} \equiv \Psi_{l::c}$.

Our contributions follow closely an early treatise on multifractal measures presented in [14]. Although uncesserily complex for the purposes of the paper, we refer the reader to [1, 31, 65] for more recent and complete formalisms.

Fractal Geometry is concerned with the study of sets that have fine-structure, i.e., detail at all scales [15]. Often these sets are also (either exactly or statically) *self-similar*, which is to say that small portions of the set may be magnified and distorted in such a way as to resemble the set as a whole. Typically, one can generate such sets by means of simple, iterative procedures [15].

A self-similar set $\mathbb{I} \subseteq \mathbb{R}$ can thus be partitioned into N equal parts scaled by a factor $r = \frac{1}{N^{-D}}$. It is illustrative to consider the following identity:

$$N \cdot \left(\frac{1}{N^{-D}} \right)^D = N \cdot r^D = 1,$$

where $N > 0, D \in \mathbb{R}_0^+$. This in turn implies that:

$$N = r^{-D} \iff D = -\frac{\log N}{\log r}. \quad (1)$$

For these types of sets, D is precisely the Hausdorff-Besicovitch dimension [15]. Crucially, a set is a fractal if its Hausdorff-Besicovitch dimension exceeds its topological dimension (i.e., its Lebesgue covering dimension).

In this manuscript, we will not be concerned with the strict, general definition of the Hausdorff-Besicovitch dimension. Note only that its computation is involved even for very simple sets [59]. We are however interested in good practical heuristics that either approximate it, or are at the very least proportional to it. We thus consider satisfactory that (1) has been found to serve as a good empirical prior in general [15]. Onwards, assume that a *fractal* set \mathbb{F} is any set for which the relationship in (1) can be verified at least as we count the number of sets of size r that cover \mathbb{F} , $N_r(\mathbb{F})$, as $r \rightarrow 0$. In practice, we will compute a *statistical* estimate of the dimension $\hat{D}(\mathbb{F})$ as:

$$\hat{D}(\mathbb{F}) \approx \text{slope of } (\log N_r(\mathbb{F}), -\log r)_{r \in \mathcal{R}}, \quad (2)$$

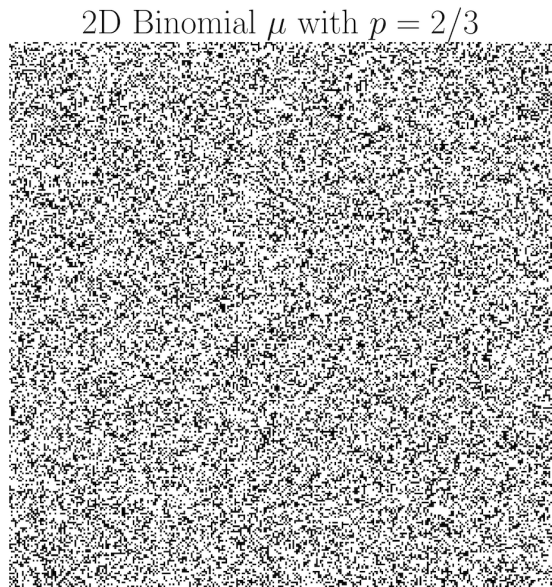
where \mathcal{R} is a finite set of discrete r . $\hat{D}(\mathbb{F})$ is the so called *box dimension* of \mathbb{F} [33]. Onwards, we will use the terms fractal and box dimension interchangeably and will refer to the theoretical Hausdorff-Besicovitch dimension explicitly if there are meaningful theoretical differences.

3.1 Multifractal formalism

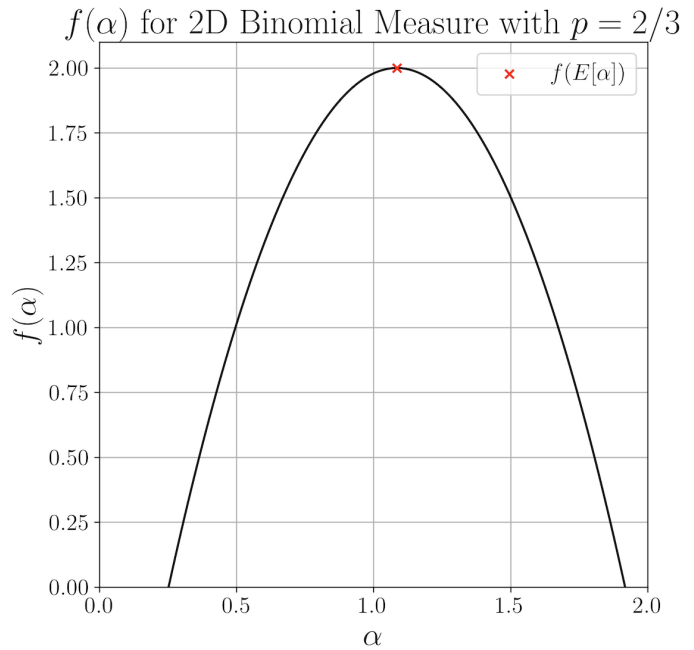
In essence, Multifractal formalism extends Fractal Geometry from sets to measures [14]. These measures may be supported on some Euclidean or fractal set.

Consider a measurable space $(\mathbb{I}, \mathcal{B}(\mathbb{I}), \mu)$, where \mathcal{B} is a Borel σ -algebra. Should the measure μ be self-similar, its value in an open ball of radius r , $B_r \in \mathcal{B}(\mathbb{I})$, is expected to *roughly* have a power relationship with α , i.e., $B_r \sim r^\alpha$. However, now we are envisioning that more than one scaling exponent may govern μ , so it is instructive to construct a self-similar measure and observe the cases where the term *multifractal* becomes necessary. Specifically, we will focus on the multinomial measures.

Suppose that $\mathbb{I} = [0, 1]$, but μ will assign mass according to some parameter $p \in [0, 1]$ at $\mathbb{I}_0 := [0, 2^{-1})$ (left) and $(1 - p)$ at $\mathbb{I}_1 := [2^{-1}, 1)$ (right). We will extend this inductively and construct a binomial expansion \mathbf{w}_k for each dyadic interval by marking the left and right expansions with 0 and 1, respectively. Inductively, let $\mathbb{I}_{k+1} = \mathbb{I}_{k0} \cup \mathbb{I}_{k1}$, and collect all possible expansions on $\mathbf{w}_k = (w_1, w_2, \dots, w_k)$, $w_i \in \{0, 1\}$. Then at *scale* k , the measure will be defined in the following collection $\mathbb{I}_{\mathbf{w}_k} := \cup_i [i2^{-k}, (i+1)2^{-k})$, where $\mathbf{w}_k = (w_1, w_2, \dots, w_i, \dots, w_{2^k})$, $w_i \in \{0, 1\}$. Note that we choose by convention the expansion with infinitely many zeroes to account for dyadic points (i.e., all $x = \frac{m}{2^{-k}}$, where m and k are integers). Then, by construction:



Distribution of μ at scale 2^{-2}



Distribution of μ at scale 2^{-4}

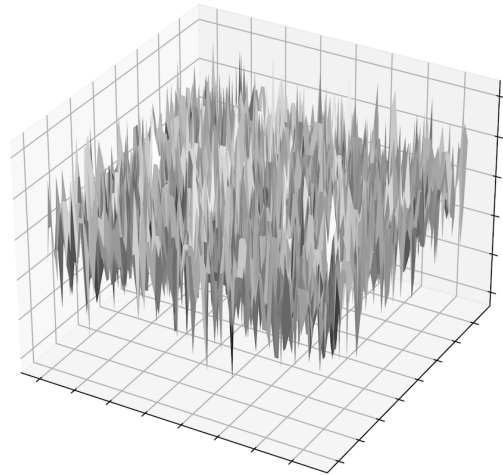
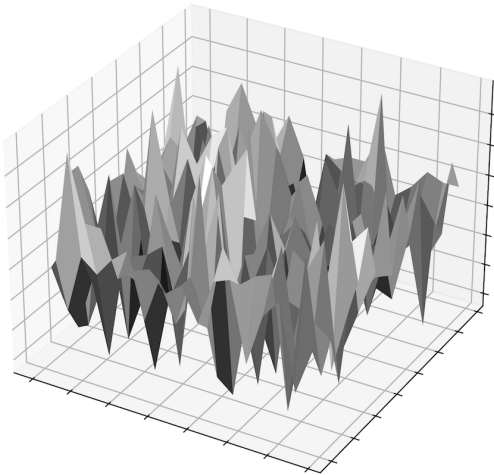


Figure 2: (Top-left) The realization of binomial measure μ with $p = 2/3$ supported in 2-dimension Euclidean space. (Top-right) The associated multifractal spectrum. Notice that f is a concave parabola and μ is singular, but $f(E_x[\alpha(x)])$ will still be associated with the dimension of the support of μ which is 2. (Bottom-left+right) 3D visualization of distribution of the μ at two different scales 2^{-k} , $k = \{2, 4\}$. Notice how the surface of μ appears to be more irregular as k increases.

$$\mu(\mathbb{I}_{\mathbf{w}_k}) = p^{n_0(\mathbb{I}_{\mathbf{w}_k})}(1-p)^{k-n_0(\mathbb{I}_{\mathbf{w}_k})}, \quad (3)$$

where $n_0(\mathbb{I}_{\mathbf{w}_k})$ denotes the number of zeroes in \mathbf{w}_k . Note that $\mathbb{I}_{\mathbf{w}_k} \in \mathcal{B}(\mathbb{I})$, for any \mathbf{w}_k .

Formally, if for some function g evaluated at arbitrary x there exists r, x_0 and C so that:

$$\alpha(x) = \sup_{|x-x_0| \leq r} \{\alpha' : |g(x) - g(x_0)| \leq C|x - x_0|^{\alpha'}\}, \quad (4)$$

then $\alpha(x)$ is *Hölder exponent* or *singularity strength* of μ at scale r around x [12, 14]. Hölder regularity is also often expressed as the distance of $f(x)$ to a polynomial $P(x-x_0)$ with degree $k < \alpha$ [31]. Intuitively, having well-defined bounded derivatives up to order α means that the function tends to vary more smoothly, whereas we expect functions with smaller values of α (especially for $\alpha < 1$) to behave more irregularly. It also means that the function will behave in a scale-free fashion around x with exponent $\alpha(x)$.

For our purposes, α_r is the value (5) within a r -neighbourhood around x . This neighbourhood is a set $\mathbb{I}_r \in \mathcal{B}(\mathbb{I})$ and we assume that $x \in \mathbb{I}_r \implies \alpha_r(x) \approx \alpha(\mathbb{I}_r)$. If μ is self-similar at x , then we expect to derive $\alpha(x)$ by observing $(\alpha_r(x), x)$ for increasingly small discrete r , and estimate this quantity analogously to (2), which is commonly demoninated as *local Hölder exponent* or *singularity strength* [14, 20, 71]:

$$\alpha_k(x) \sim \frac{\log \mu(\mathbb{I}_{\mathbf{w}_k})}{\log 2^{-k}}. \quad (5)$$

The value of $\mu(\mathbb{I}_{\mathbf{w}_k})$ depends solely on p and $n_0(\mathbb{I}_{\mathbf{w}_k})$. In practice, the coarse local Hölder exponent at x is computed by evaluating (5) at several *scales* k and an estimate estimate is produced analogously to (2).

The concept of a multifractal measure becomes clear when one observes that μ is exactly the *Binomial* measure. Specifically, that the number of points that scale with α , $N_k(\alpha)$, can be attained by computing the binomial expansion, and thus:

$$N_k(\alpha) = \binom{k}{n_0(\alpha_k)k} \sim (2^{-k})^{-f(\alpha_k)}, \quad (6)$$

so that $f(\alpha) = -\log_2(n_0(\alpha)^{n_0(\alpha)}(1-n_0(\alpha))^{1-n_0(\alpha)})$, by leveraging Stirling's approximation [14]. This relation $N_k(\alpha) \sim r^{-f(\alpha_k)}$, is homologous to (1). For measures where such a relation holds, the value of $f(\alpha)$ will exactly be the Hausdorff-Besicovitch dimension of the following level set [14, 71, 72]:

$$\mathbb{I}^\alpha = \{x \in \mathbb{I} : \alpha(x) = \alpha\}. \quad (7)$$

Since f maps α to a spectrum of fractal dimensions of \mathbb{I}^α , it is henceforth called the *multifractal spectrum* (MFS).

These relations can be derived for the more general Multinomial measures parameterized by m parameters so that $\mu(\mathbb{I}_{\mathbf{w}_k}) = \prod_{i=1}^m p_i^{n_i(\mathbb{I}_{\mathbf{w}_k})}$ [14]. There are also other ways of computing f by using Wavelet transforms or by detrended fluctuation analysis (DFA), and we recommend [59] for an in-depth overview of these methods.

Our contribution relates more closely with the *Histogram Method* given that we are focusing on imaging modalities. Empirical results appear to favor the method in this context of Computer Vision, especially if one computes several different measures (i.e., filters) over the same *static* phenomena (i.e., image) [63, 71, 19]. There are also other ways of computing f by using Wavelet transforms or by DFA, and we recommend [59] for an in-depth overview of these methods

The *Method of Moments* is arguably more adopted in general. It uses the *Legendre* transform to write f and α as functions of the normalized moments q of μ , $\tau(q)$:

$$f(\alpha(q)) = q\alpha(q) - \tau(q) \text{ where } \alpha(q) = \frac{\partial \tau(q)}{\partial q}, q \in \mathbb{R}. \quad (8)$$

It is also pivotal for defining the *set of generalized dimensions* D_q , and the interested reader is referred to [21, 33] for additional details. For this paper, we mainly use the link between D_q and $f(\alpha)$ as a convenient formal construct for our proofs.

3.2 Squeeze-and-Excite [22]

Squeeze and excitation networks (SE) were originally studied by [58], and we will onward use the the acronym cSE (channel SE) for consistency with medical image segmentation literature, even though cSE and SE are functionally equivalent.

The output of each encoder layer Ψ_l is characterized by a “squeeze” function $g : \mathbb{I}_l \rightarrow \mathbb{R}^{C_l}$ such that:

$$g(\Psi_l(\mathbf{X})) = \sigma(\mathbf{W}_2 \text{ReLU}(\mathbf{W}_1 \text{GAP}(\Psi_l(\mathbf{X})))), \quad (9)$$

where GAP denotes spatial global average pooling, $\mathbf{W}_1 \in \mathbb{R}^{\lfloor \frac{C_l}{s^*} \rfloor \times C_l}$, $\mathbf{W}_2 \in \mathbb{R}^{C_l \times \lfloor \frac{C_l}{s^*} \rfloor}$, for some $1 \leq s^* < C_l$, and σ is the sigmoid activation function. The output of the encoder at level l for $l < L - 1$ thus becomes:

$$\Psi_l^{\text{Excited}}(\mathbf{X}) = \Psi_l(\mathbf{X}) \odot g(\Psi_l(\mathbf{X})), \quad (10)$$

where \odot is the (broadcastable) element-wise product.

3.3 Spatial and Channel SE[?]

For the purposes of semantic segmentation of medical images, it is proposed to perform the squeeze operator along the spatial dimensions, in order to have an attention function with the original feature map resolution.

The authors propose an additional branch, where the pooling operator of (9) is replaced by a learnable 1×1 convolution layer, producing $g^{\text{Spatial}}(\Psi_l(\mathbf{X}))$. The authors propose the final activations to be

$$\Psi_l(\mathbf{X}) = \max(\Psi_l(\mathbf{X}) \odot g(\Psi_l(\mathbf{X})), \Psi_l(\mathbf{X}) \odot g^{\text{Spatial}}(\Psi_l(\mathbf{X}))), \quad (11)$$

where \max is performed element-wise, i.e., the function is a maxout layer [17].

3.4 Style-based Recalibration [38]

Style-based Recalibration (SRM) integrates the standard deviation as a proxy for style in the context of style-transfer. Denoting a global standard-deviation pooling layer as GSP, the squeeze function is defined as:

$$g(\Psi_l(\mathbf{X})) = \phi([\text{GAP}(\Psi_l(\mathbf{X})), \text{GSP}(\Psi_l(\mathbf{X}))]), \quad (12)$$

where $\phi : \mathbb{R}^{C_l \times 2} \rightarrow \mathbb{R}^{C_l}$ is a learnable linear map. An additional batch-normalization layer is applied to g .

3.5 Frequency Channel Attention [53]

Frequency Channel Attention networks (FCA) were designed to generalize the “squeeze” operation in SE.

The authors observe that global average pooling acting on feature maps of fixed spatial dimensions is a special case of of the Discrete Cosine Transform (DCT). More precisely, it is equal to the lowest frequency component up to a fixed constant factor [53]. FCA thus enables to use the entirety of the DCT transform to describe feature maps by partitioning each layer in k groups, whereupon action of a distinct DCT basis is estimated.

Specifically, the C_l channels of each layer l in are split into k groups such that $[\Psi_l(\mathbf{X})_1, \dots, \Psi_l(\mathbf{X})_k] = \Psi_l(\mathbf{X})$. The two-dimensional DCT filters are pre-computed and stored on a tensor \mathbf{B} :

$$\mathbf{B}_{l,h,w}^{i,j} = \cos\left(\frac{\pi h}{H_l}\left(i + \frac{1}{2}\right)\right) \cos\left(\frac{\pi w}{W_l}\left(j + \frac{1}{2}\right)\right). \quad (13)$$

The squeeze operation is performed for each of the k groups:

$$g(\Psi_l(\mathbf{X}))_k = \sum_h \sum_w \Psi_l(\mathbf{X})_k B_{l,h,w}^{i_k, j_k}, \quad (14)$$

i_k, j_k depend on k since ensuring a distinct DCT basis for each of the k groups $g(\Psi_l(\mathbf{X})) := \sigma(\mathbf{W}[g(\Psi_l(\mathbf{X}))_1, \dots, g(\Psi_l(\mathbf{X}))_k])$, so that $\mathbf{W} \in \mathbb{R}^{C_l \times C_l}$.

4 Methods

We look at the l -th output of encoder head $\Psi_l = [\mu_{l_{c_1}}, \dots, \mu_{l_{C_l}}]$, $\mu_{l_c} \geq 0$, i.e., a tensor of unnormalized measures (filters) that we assume are meaningful for the downstream task. We adjust the responses of the encoder using *learnable functions* of the local (multifractal) or global (monofractal) interactions between the singularity strengths derived across each channel/measure of f_l . We start by demonstrating that the proposed recalibration functions indeed relate to quantities that relate to $f(\alpha)$.

Our proofs will consider measures $\nu = (\mu_q)_{q=1}^Q$ that take the multinomial form. By construction, each μ_q is a binomial measure with potentially unique support and we model and let $p^{(q)}(\alpha^{(q)})$ be the normalized density of each exponent in ν so that:

$$p(\alpha_\nu) := [p^{(1)}(\alpha^{(1)})/Z, \dots, p^{(Q)}(\alpha^{(Q)})/Z], \quad (15)$$

where $Z = \sum_q p^{(q)}(\alpha^{(q)})$. Note however that these multifractal measures have enjoyed great success in practice [33, 19]. We also introduce learnable parameters in their implementation, thus allowing to characterize the scaling nature of other multifractal phenomena beyond multinomial cascades.

4.1 Differentiable scaling exponent computation

As mentioned in Section 3.1, the Hölder exponent can be computed in an analogous fashion to the fractal dimension (2). Defining a finite scale set $\mathcal{R} = \{k_1, \dots, k_r : i < j \implies k_i < k_j\}$, we can derive the following dyadic cubes $[i_h - 2^{-k}, i_h + 2^{-k}) \times [i_w - 2^{-k}, i_w + 2^{-k})$. For a cube $B_k(x)$ centered on x we can approximate the local singularity strength for the c -th channel of the l -th layer as the power-law relationship manifested at finitely many resolutions k . We approximate the local Hölder (5) exponents by solving:

$$\alpha(x) \approx \text{slope of } (\log \mu(B_k(x)), \log k)_{k \in \mathcal{R}},$$

for all x . Concretely, we attain this value through the ordinary least squares solution:

$$\alpha(x) = \frac{\sum_k \left(\log \mu(B_k(x)) - \frac{1}{|\mathcal{R}|} \sum_{k'} \log(\mu(B_{k'}(x))) \right)}{\sum_k \left(\log k - \frac{1}{|\mathcal{R}|} \sum_{k'} \log k' \right)}. \quad (16)$$

In our implementation, $\mu(B_k(x))$ is computed by convolving each Ψ_{lc} with a kernel of ones of size k and stride 1 (a static depth-wise convolution layer in practice). This operation extends trivially to tensor operations, so $\alpha_{lc}(x)$ can be efficiently computed by performing this operation in a depth-wise convolution layer, readily available in modern deep learning frameworks ².

4.2 Fractal-based Recalibration

Recalling the notation set on the Section 3, suppose we collect each Hölder exponent in:

$$\boldsymbol{\alpha} := (\alpha_k(x))_{x \in \text{supp } \mu} \quad (17)$$

and let $\alpha_k(\cdot)$ be an approximation of (16) using resolutions $\mathcal{R} = \{1, \dots, 2^{-k}\}$.

Theorem 4.1 (Fractal recalibration). *Suppose that μ is a multinomial measure as in equation (15) with multifractal spectrum f , then almost surely (a.s.) for $\mathcal{R} = \{1, \dots, k\}$ for sufficiently large k :*

$$\mathbb{E}_x[\boldsymbol{\alpha}] \propto D(\text{supp } \mu),$$

where D is the box-dimension of the support.

Proof: We prove the non-trivial case for non-singular multinomial measures using an argument similar to Evertsz and Mandelbrot [14, Section 2.4]. By definition $\mu(\mathbb{I}) = 1$ and so $\mu(\mathbb{I}^\alpha) \leq \mu(\mathbb{I})$. Note also that $\mu(\mathbb{I}^\alpha) = r^{-f(\alpha)} r^\alpha \leq 1$ (refer to (6)), and thus it must be that $f(\alpha) \leq \alpha$. For multinomial measures, $f(\alpha)$ is concave. Also for this case, and referring back to the Legendre transform in (8), we can assume $q \geq 0$, so the exponent α that maximizes f needs to verify $\frac{\partial f(\alpha(q))}{\partial \alpha} = 0$ — this extremum is a maximum if and only if $q = 0$, which is equivalent box dimension of the support of the measure [33]. Referring back to the shape of f (see Eq. (6) or Figure 2), clearly $\mathbb{E}[\alpha]$ maximizes $f(\alpha)$.

In order to show that the expectation over x relates to this quantity, we again extend the arguments of Evertsz and Mandelbrot in [14, Section 4.2]: leveraging the law of large numbers, for any $x \in \text{supp}(x)$:

$$\alpha(x) \stackrel{\text{a.s.}}{=} \mathbb{E}(\alpha), \text{ where } \alpha \text{ in the r.h.s. is in the domain of the MFS of } \mu: (\alpha, f(\alpha))$$

Denoting $|\text{supp } \mu| = n \in \mathbb{R}^+$, it follows that $\mathbb{E}_x[\boldsymbol{\alpha}] \stackrel{\text{a.s.}}{=} n^{-1} D(\text{supp } \mu)$ □

4.2.1 Monofractal recalibration

This theorem provides a fundamental explication to empirical observations: estimations of α tend not to vary meaningfully in the support of the measure [33, 59].

Remark 4.2 (Monofractal recalibration). If μ is uniform and supported on fractal set \mathbb{F} , μ is said to be monofractal, i.e., it is governed by a single scaling exponent. Under these conditions, the multinomial measure will reduce to the Lebesgue measure λ . However, $\mathbb{E}[\alpha(x)] \propto D(\mathbb{F})$ as in (1), even though $\lambda(\mathbb{F}) = 0$.

²E.g., PyTorch through `torch.nn.Conv2d` (with `groups=in_channels`) or TensorFlow's `DepthWiseConv2D`.

Proof: The probability mass is uniform so $\mu(\mathbb{I}^{\alpha_i}) = \mu(\mathbb{I}^{\alpha_j})$ for any i, j , i.e., the mass is evenly distributed with respect to the terms of the the m -ary expansion of any x , and so $\mathbb{I} = \{\alpha : x \in \text{supp } \mu\}$. The MFS thus collapses to a single value α , which can be recovered using the expectation operator in Theorem 4.1. \square

4.2.2 Multifractal recalibration

The previous recalibration strategy is suitable for when each (learned) measure μ is well characterized by a monofractal. Notwithstanding, it does not characterize the entirety of the MFS, it can only capture a value associated with the dimension of its support.

Remember from Section 3.1 that $f(\alpha)$ is the *Haurdorff-Besicovich* dimension of \mathbb{I}^α . We know that $\mu(\mathbb{I}^\alpha) = N_k(\alpha)(2^{-k}) \sim 2^{-f(\alpha)+\alpha}$. If one treats the Hölder exponent of a binomial cascade at the k -th scale α as a random variable, then by the Gaussian Central Limit theorem, for sufficiently large k , the following two statements hold [14]:

$$p_k(\alpha) \propto \exp \left\{ \frac{1}{2} \left(\frac{\alpha - \alpha_0}{\sigma/\sqrt{k}} \right)^2 \right\} \quad (18)$$

around most probable scaling exponent α_0 . Recall that $\mathbb{E}_x[\alpha] \rightarrow \alpha_0$ as $k \rightarrow \infty$. Should μ be supported on a set with Hausdorff-Besicovich dimension D [14]:

$$f_k(\alpha) \approx D + \frac{1}{k} p_k(\alpha). \quad (19)$$

Hence, for our purposes, it is fair to assume that the support has fixed dimension, so our inductive bias can be on p_k , since $p_k \propto f_k$.

It is also very possible that some phenomena may not be aptly described solely by this quantity. Indeed the conditional likelihood of the singularities may vary depending on the context. We set forth *Multifractal Recalibration* to address this issue, assuming there the quantity we want to model may also depend on the context (i.e., the desirable mapping $\mathbf{X} \mapsto \mathbf{Y}$).

Definition 4.3 (Data-dependent multinomial measure). Suppose we build μ^* by weighing multinomial μ as a function of a labeling function $l : \mathbb{I} \rightarrow \{0, 1\}$ defined as the restriction $\mathbb{Y} = \{x \in \mathbb{I} : l(x) = 1\}$. Then, the data-dependent multinomial measure is given by:

$$\mu^*(\mathbb{I}) = \frac{\mu(\mathbb{I} \cap \mathbb{Y})}{\mu(\mathbb{Y})}$$

Note that μ^* has the same scaling behaviour as μ , but it assigns all mass to restriction \mathbb{Y} .

Remark 4.4 (Multifractal recalibration). Consider all points x in some level set indexed by q , i.e., $\mathbb{I}^{\alpha(q)} \subseteq \mathbb{I} = \{x : \alpha(x) = \alpha(q)\}$ ³. Consider measures μ, μ^* supported on \mathbb{I} , the latter being constructed from μ and some labeling function $l(x)$. Then any measure $\hat{\mu}$ that verifies:

$$\hat{\alpha} = \arg \max_{\alpha'} \frac{1}{Z} \exp(-(\alpha' - \alpha^*)^2),$$

has to have perfect level-set likelihood ratio $\frac{\hat{\mu}(\mathbb{I}^{\alpha(q)})}{\mu^*(\mathbb{I}^{\alpha(q)})} = 1 \forall q$, where $Z = \int \exp\{-(\alpha' - \alpha^2)\} dq$.

³Using index q is merely evocative, but not equivalent to, using the Legendre transform.

Proof: According to the definition of coarse Hölder exponent (5), for any x, q such that $x \in \mathbb{I}^{\alpha(q)}$:

$$\alpha'_q(x) := \frac{\log \mu'(\mathbb{I}^{\alpha(q)})}{\log 2^{-k}} \text{ and } \alpha_q^*(x) := \frac{\log \mu^*(\mathbb{I}^{\alpha(q)})}{\log 2^{-k}}.$$

For sufficiently large fixed k , we can disregard the denominators. Moreover, since Z does not depend on q , pick arbitrary $\alpha(q)$:

$$\begin{aligned} \alpha'_q(x) - \alpha_q^*(x) &\approx \log \mu'(\mathbb{I}^{\alpha(q)}) - \log \mu^*(\mathbb{I}^{\alpha(q)}) \\ \implies \exp \left\{ - \left(\log \mu(\mathbb{I}^{\alpha(q)}) - \log \mu^*(\mathbb{I}^{\alpha(q)}) \right)^2 \right\} &= \exp \left\{ - \left(\log \frac{\mu'(\mathbb{I}^{\alpha(q)})}{\mu^*(\mathbb{I}^{\alpha(q)})} \right)^2 \right\}. \end{aligned}$$

Thus the maximizer α' of the above stated Gaussian function must have level-set likelihood ratio $\frac{\mu'(\mathbb{I}^{\alpha(q)})}{\mu^*(\mathbb{I}^{\alpha(q)})} = 1$ for all q . \square

4.3 Implementation

Our implementations are grounded on Theorem 4.1 and its instantiation in the mono (4.2) or multifractal (4.4) cases.

We adapt the notation set on (17) to the case where we collect the Hölder exponents captured in the c -th filter of the l -th layer, given the output of $\Psi_l(\mathbf{X})$:

$$\mathbf{H}_l \in \mathbb{R}^{H_l \times W_l} := [\alpha(\Psi_{lc}(x))], \text{ for all } x \in \text{supp } \mu. \quad (20)$$

and and suppose we compute $\alpha(\cdot)$ using (20) with a resolution of $r = 2^{-k}$.

The outputs of (20) are not normalized, which can compromise optimization during gradient descent [10, 25]. Thus, onwards \mathbf{H}_l signifies the empirical singularity exponents after the action on a *distinct* batch-normalization layer for each l .

In order to recalibrate the response for the monofractal case we need to determine each filter's box-dimension. The expectation in 4.1 is performed for each channel of \mathbf{H}_l , and the global descriptor is then fed to a squeeze-and-excitation pathway [22]. The output of Ψ_l will be recalibrated by a function $g : \mathbb{I}_l \rightarrow \mathbb{R}^{C_l}$:

$$g^{\text{Mono}}(\Psi_l(\mathbf{X})) = \sigma(\mathbf{W}_2 \delta(\mathbf{W}_1 \text{GAP}(\mathbf{H}_l))), \quad (21)$$

$\mathbf{W}_1 \in \mathbb{R}^{\lfloor \frac{C_l}{s^*} \rfloor \times C_l}$, $\mathbf{W}_2 \in \mathbb{R}^{C_l \times \lfloor \frac{C_l}{s^*} \rfloor}$, for some $1 \leq s^* < C_l$, and σ, δ are the sigmoid and rectified linear unit (ReLU) activation functions, respectively. The output of the encoder at level l for $l < L - 1$ thus becomes:

$$\Psi_l^{\text{Mono}}(\mathbf{X}) = \Psi_l(\mathbf{X}) \odot g^{\text{Mono}}(\Psi_l(\mathbf{X})). \quad (22)$$

This response is propagated to Ψ_{l+1} , but also to the decoder in case of the U-Net by means of a skip connection.

As mentioned in the previous section, the above recalibration strategy can only capture one scaling exponent per filter. Moreover, it does not account for likely fact that our estimate of μ_{lc} likely does not meet the conditions of maximization in some downstream task. In other words, we expect our representation Ψ to characterize the entirety of the input $\mathbf{X} \sim \mu$ and not necessarily distribute the mass across each level-sets as a function of our dependant variable of interest $\mathbf{Y} \sim \mu^*$.

To achieve this data-dependant recalibration stated in 4.4, we allow Q learnable scaling exponents to be learned in gradient descent, so that $\mathbf{H}_l^* \in \mathbb{R}^Q$. These exponents induce Q level-sets, so that:

$$p^{(q)}(\alpha(x)) \propto \exp(-s_q^*(\alpha(x) - \mathbf{H}_{l_q}^*)^2),$$

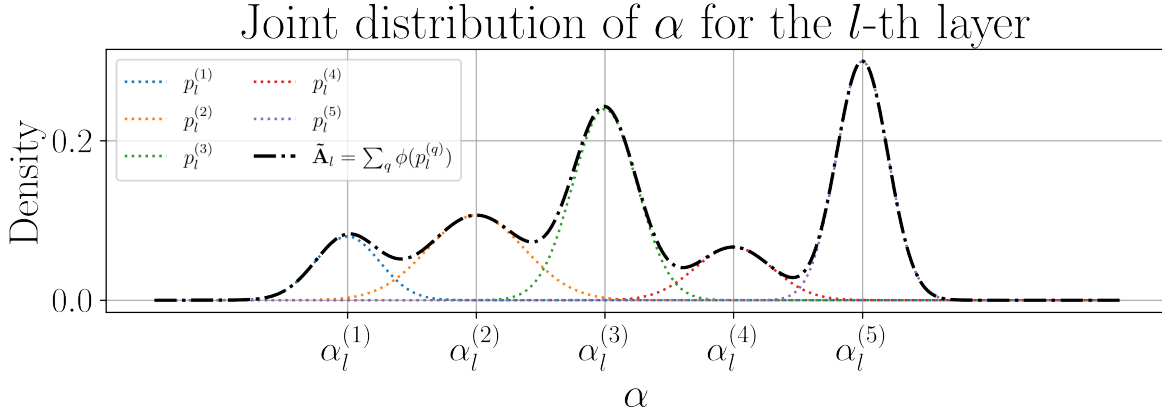


Figure 3: Visualization of the joint encoding of p_l at encoder Ψ_l . Each level set is characterized by a Gaussian $p_l^{(q)}$ localized around $\alpha_l^{(q)}$.

where the decay around the peak of each level-set is modulated by $(s_q^*)^{-1}$, which will vary as the empirical and data-dependent exponents diverge.

Its general formulation to account for input $\Psi(\mathbf{X})$ is expressed via the following softmax function:

$$p_l^{(q)}(\mathbf{H}_l) \propto \frac{\exp(-s_q^*(\mathbf{H}_l - \mathbf{H}_{lq}^*)^2)}{\sum_{q'} \exp(-s_{q'}^*(\mathbf{H}_l - \mathbf{H}_{lq'}^*)^2)}, \quad (23)$$

where $q \in \{1, \dots, Q\}$, and $s_q^* \in \mathbb{R}$, $\mathbf{H}_l^* \in \mathbb{R}^Q$ are learnable parameters. Each layer Ψ_l is thus partitioned in Q stochastic level sets, i.e., there is parameter sharing across spatial and channel axes. This expression closely resembles the context-encoder functions leveraged in [75, 72].

The morphology of the MFS in this recalibration function is also relaxed due to the data-driven partitioning of \mathbb{I}_l , which is desirable when the MFS morphology differs from a perfect concave parabola [14, 12, 20].

We surmised that each stochastic level set defined in (23) should be weighted differently depending on the downstream task. We opt for a weighted sum aggregation and learn an orderless pooling function over q , a common approach in texture classification [75, 72, 11]. We propose to pool the response of \mathbf{H}_l across the Q -axis, using a batch-normalization layer ϕ , so that:

$$\tilde{\mathbf{H}}_l := g^{\text{Multi}}(\Psi_l(\mathbf{X})) = \sigma \left(\sum_q \delta(\phi(p_l^{(q)}(\alpha_l^{(q)}))) \right), \quad (24)$$

where σ, δ are the sigmoid and ReLU activation functions, respectively. Without the activation functions, this aggregation is a mixture of Q Gaussians (as in Figure 3).

The final step is to fuse this representation with the response of Ψ_l . We found that an element-wise sum strategy similar to [76] to be particularly effective:

$$\Psi_l^{\text{Multi}}(\mathbf{X}) = \Psi_l(\mathbf{X}) + \tilde{\mathbf{H}}_l, \quad (25)$$

where $+$ is the element-wise sum. Note that, by the linearity of convolution, $\Psi_{lc}^{\text{Multi}} * \mathcal{D}_{lc} = (\Psi_{lc} * \mathcal{F}_{lc}) + (\tilde{\mathbf{H}}_{lc} * \mathcal{F}_{lc})$, so in this way we ensure that singularity information may be easily disentangled by the decoder filter \mathcal{D}_{lc} .

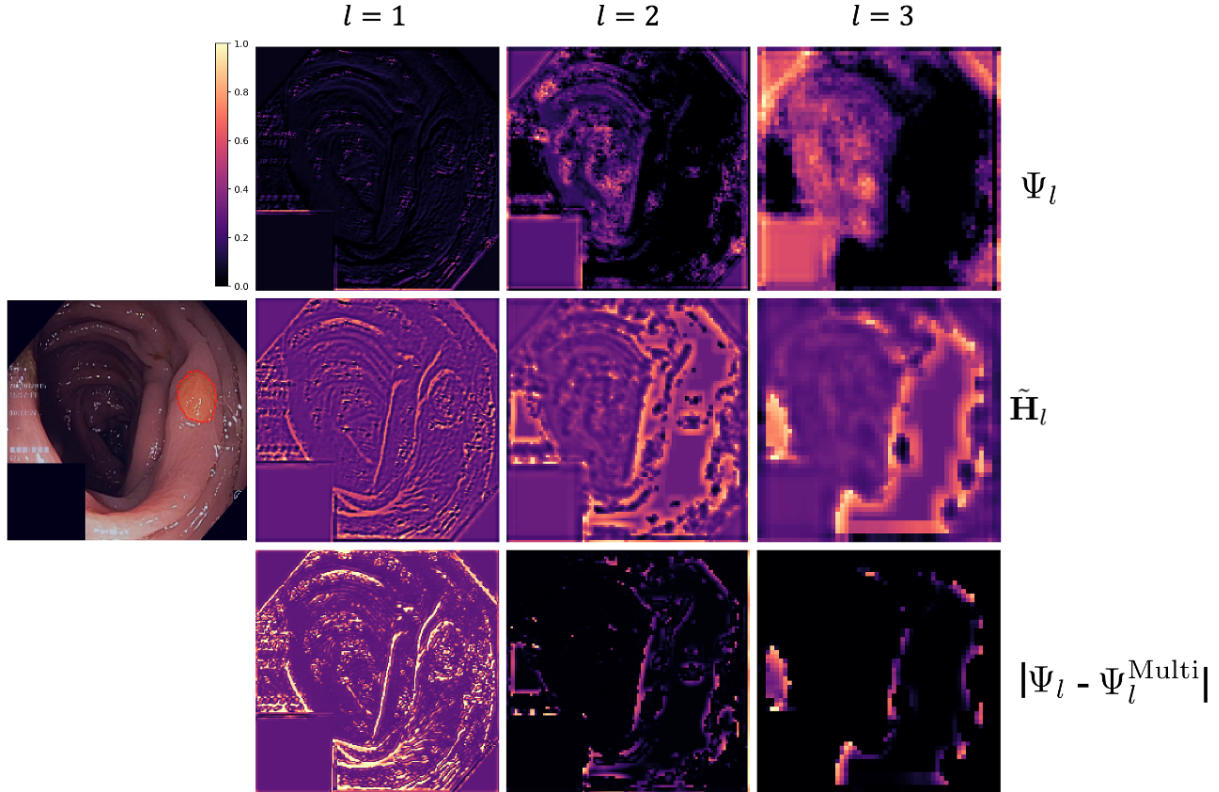


Figure 4: (Left-most) The input KvasirSEG image (from validation set) and target region of interest (highlighted in red). (Right) Layer depth $l \in \{1, 2, 3\}$ versus normalized response of Ψ_l , $\tilde{\mathbf{H}}_l$, and $|\Psi_l - \Psi_l^{\text{Multi}}|$. Note how $\tilde{\mathbf{H}}_l$ encodes complementary textural information of Ψ_l for $l = 1$. For $l = 2, 3$ the preferred singularities relate more to luminance changes that highlight anatomical structures. This also illustrates the theory set forth by Vehel et al. [63], where each level set is associated with a distinct visual primitive.

5 Experiments

5.1 Materials

We conducted experiments in three different public datasets from medical imaging modalities that vary significantly in terms of equipment and interventions used. These modalities also present challenging multi-scale characteristics, as well as variations in intensity, lighting, noise artifacts, and texture. Specifically, we selected the ISIC18 (dermoscopy [13]), KvasirSEG (endoscopy) [32], and BUSI (breast ultrasound) [2] datasets. As discussed in [27], using three datasets is the median number of recent contributions towards general models for medical image segmentation, provided that the datasets are varied and of sufficiently high quality (i.e., low inter-method and high intra-method variability).

5.2 Experimental setup

As prescribed by [27] we enforce a 5-fold cross-validation setup for all datasets. For each fold, we leave out 10% of each train partition to be used for early stopping. For the case of the BUSI dataset, each split is always stratified over the pathological classification variable since the ratio of benign

to align samples is roughly 2:1 [2]. For all datasets, all image/mask pairs were down-sampled to a 224×224 spatial resolution using bilinear interpolation and then normalized to have channel values in $[0, 1]$. Standard data augmentation was enforced using random horizontal and vertical flips, each with $p = 0.5$.

We validate our approaches against the original SE module [22], the concurrent spatial and channel squeeze + channel excitation (scSE) proposed in [58], the SRM [38], and the FCA [53] module. For FCA we used the best static configuration comprised of the 16 coefficients associated with the lowest frequencies of the DCT base [53]. Other than scSE and Multifractal recalibration, we call the other attention function *global* channel attention functions since they do not recalibrate filter responses at the “pixel level”.

We use the same baseline as [4], comprised of three encoder/decoder pairs with 32, 64, and 128 channels, and a bottleneck of 256 channels. In cSE, scSE, FCA, and Monofractal recalibration, the MLP architecture is the same, and we set $r^* = 2$ following [58]. For our proposed approaches, we set $\mathcal{R} = \{2, 3, 4\}$ to compute \mathbf{H}_l (see Section 4). For Multifractal recalibration we learn $Q = 16$ stochastic level sets.

Our main research question is whether we can integrate the *multifractality* of \mathbf{X} end-to-end to predict \mathbf{Y} . However, our target variables \mathbf{Y} are very regular, even on the borders, likely due to limitations in the annotation procedures (see Fig. 5). We contend that, in isolation, the decoder is not explicitly encouraged to approximate an irregular function. With this in mind, and in order to streamline our experimental processes, we study the impact of the recalibration functions solely after each encoder output (before skip-connection and max-pooling as in [58, 51, 55]).

All models were trained using a mini-batch size of 16. Note that this value is empirically found to be the smallest mini-batch size that ensures that the modules that leverage batch normalization are not at a disadvantage [68]. The Adam gradient descent algorithm [34] was used with an initial learning rate of 1×10^{-4} over 400 epochs. A scheduler adjusted the learning rate by a factor of 0.5 should a plateau of the training procedure be detected with a patience of 10 epochs. We ensured that these fixed experimental parameters allowed all models to converge. All models were evaluated in terms of their Dice-Sørensen score.

5.3 Results

The 5-fold experiments reveal that at least one of the proposed approaches always outperforms all others for all datasets (see Table 1). Both cSE and Multifractal recalibration are always beneficial on average when compared to the baseline. However, Multifractal recalibration is the only approach that improves the baseline in a statistically significant manner throughout all datasets. Both of the proposed approaches simultaneously show superior performance to all others in the ISIC18 and BUSI datasets.

It is important to analyse how one should weigh the evidence per dataset, so following [27] we analyze the ratios of intra an inter-model standard deviation for each dataset (see Figure 6). Both ISIC18 and Kvasir-SEG are above the threshold where the inter-model variance is of a higher average magnitude than intra-model. BUSI is below this threshold, but it is the only dataset where all of the approaches displayed a dramatic improvement over the baseline, with the highest differences being for SRM and Monofractal recalibration, +5.89% and +6.8% Dice, respectively. This dataset is thus less reliable for assessing differences between attention functions, but it is still valid to show that attention functions can improve baseline performance drastically for this task.

It is noteworthy that our approaches are always superior to FCA, which is the most intricate statistical channel descriptor. SRM also captures second-order information, but it is only competitive in the BUSI dataset, and fails to even match baseline performance in the other cases.

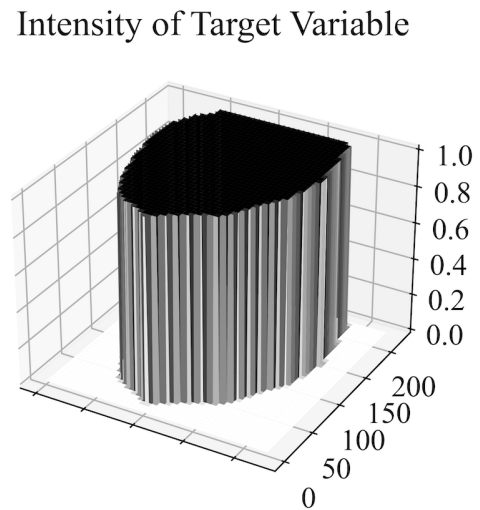
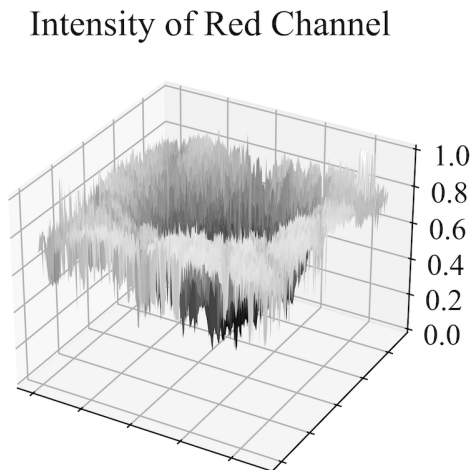
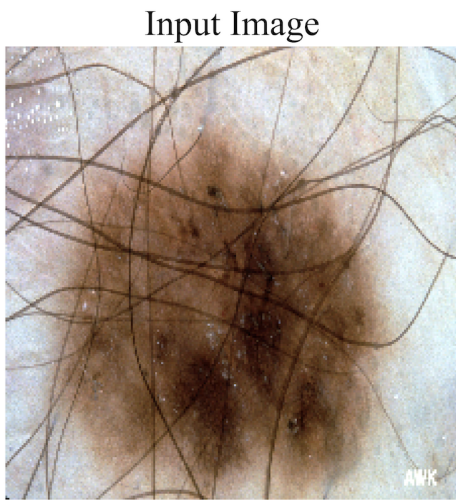


Figure 5: The intensity distribution of the input is highly irregular. Conversely, the target variable is very homogeneous and only relates information of the general region of interest. Sample taken from the ISIC18 dataset.

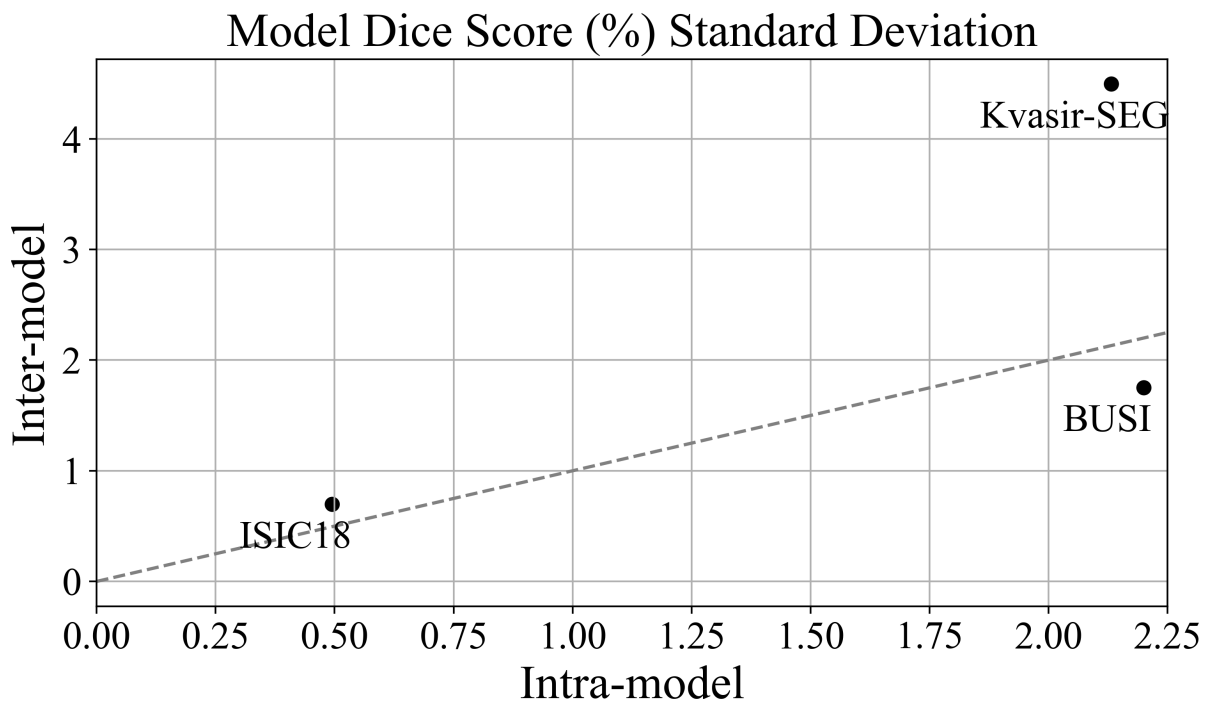


Figure 6: Dice score (%) inter and intra-model standard deviation per dataset. The dashed gray line marks a ratio of inter/intra model variability of 1.

Table 1: Mean \pm standard deviation Dice score (%) of the cross-validation experiments. \cdot^\dagger and \cdot^\ddagger signify that the null-hypothesis of the pairwise t-test with regards to the U-Net baseline is rejected with $p \leq 0.05$ and $p \leq 0.01$, respectively. Best mean results are boldfaced.

| Model | ISIC18 | Kvasir-SEG | BUSI |
|---------------|--|---|--|
| U-Net [57] | 85.40 \pm 0.25 | 72.22 \pm 1.82 | 62.20 \pm 2.40 |
| +cSE [22] | 85.94 \pm 0.36 † | 72.72 \pm 1.52 | 65.36 \pm 1.36 |
| +scSE [58] | 85.92 \pm 0.29 † | 72.94 \pm 1.07 | 64.82 \pm 1.03 |
| +SRM [38] | 84.33 \pm 1.27 | 61.13 \pm 3.42 | 68.09 \pm 3.14 † |
| +FCA [53] | 86.19 \pm 0.75 | 70.00 \pm 2.51 | 66.27 \pm 2.48 |
| +Mono (ours) | 86.24 \pm 0.27 ‡ | 71.86 \pm 2.37 | 69.00 \pm 2.53‡ |
| +Multi (ours) | 86.26 \pm 0.28‡ | 74.76 \pm 2.20† | 66.94 \pm 2.45 † |

Table 2: Mean \pm standard deviation dice score (%) for values in $Q \in \{2, 4, 8, 16\}$ measured on the ISIC18 dataset. Best mean results are boldfaced.

| $Q = 2$ | $Q = 4$ | $Q = 8$ | $Q = 16$ |
|------------------|------------------|------------------|------------------------------------|
| 86.21 \pm 0.49 | 86.21 \pm 0.32 | 86.15 \pm 0.28 | 86.26 \pm 0.28 |

Monofractal recalibration appears to have greater impact on performance when it works well, compared to cSE and even scSE. An interesting result is that cSE was superior on average to scSE in the BUSI dataset, and coincidentally, in the same dataset, Monofractal outperformed all other approaches, including Multifractal recalibration. We hypothesize that the speckle noise present in the ultrasound images [73] might lead to local singularities that are still propagated by Ψ_l , which leads to diminishing returns faster for these spatial approaches. Keep in mind that in spite of this fact, the Multifractal approach still shows sizeable statistical significant improvement over the baseline for this dataset, and that our analysis ranks BUSI lowest with regards to distinguishing differences between extensions of the baseline U-Net (see Figure 6). Despite this, Multifractal recalibration still increased baseline Dice score significantly.

Interestingly, Monofractal recalibration alongside the other sophisticated global statistical channel attention functions (SRM and FCA) under-performed when compared not only to cSE and scSE, but also to the baseline. On the other hand, the superior performance of Multifractal recalibration in the same dataset attests to the fact that higher order statistical information is crucial for Kvasir-SEG.

We investigated what kind of information is captured in the singularity map \mathbf{H}_l associated with Ψ_l (see Figure 4). Qualitatively, the singularities appear to highlight general rugosity patterns latent in the feature maps. Multifractal recalibration effectively clusters this singularity information into macro-structures that become especially visible as $l \rightarrow L$.

5.4 Multifractal hyperparameter and aggregation analysis

In order to understand the impact of the number of soft bins in the histogram of Equation (23) we vary the value of the number Q mixtures so that $Q \in \{2, 4, 8, 16\}$. We measure the average and standard deviation of the Dice score in a 5-fold cross-validation setup of the ISIC18 dataset. The results are collected in Table 2. Most of the performance is achieved immediately at $Q = 2$ histograms. This result becomes less surprising by realizing that this method shares some commonalities with the context encoding proposed in [75], where Q is always set to the number of classes. However, contrary to [75], we do not need any additional architectural changes nor loss

terms during supervision. The increase in performance with bigger Q is not significant. However, at $Q = 16$ the average performance does increase slightly while simultaneously decreasing the amount of variance. We also found that this value of Q worked well in general for our experiments, as described in Section 5.3.

Table 3: Mean \pm standard deviation of Multifractal of activation function pooling ablation in the Kvasir-SEG dataset (Dice (%)). The best mean results are boldfaced.

| $\sum_q \phi(\cdot)$ | $\sigma(\sum_q \phi(\cdot))$ | $\delta(\sum_q \phi(\cdot))$ | $\sigma(\sum_q \delta(\phi(\cdot)))$ | $\delta(\sum_q \delta(\phi(\cdot)))$ |
|----------------------|------------------------------|------------------------------|--------------------------------------|--------------------------------------|
| 73.91 \pm 1.67 | 73.87 \pm 1.38 | 73.66 \pm 1.69 | 74.76 \pm 2.20 | 69.82 \pm 2.37 |

Next, we inquire about the design of the aggregation strategy of $\phi(p_l^{(q)}(\mathbf{H}_l))$ over axis Q . These results are collected in Table 3, which can be broken down into two parts: the choice of (non) linearity inside and outside the pooling aggregation. ReLU is the only candidate inner activation function, since it is already known to be empirically effective [75].

Two surprising facts about our results: the sigmoid in the outer activation function leads to the ultimate performance configuration, and the linear model is the second best in terms of average performance. Concerning the latter, as described in Section 4.2.2, this aggregation can be seen as a linear mixture of Gaussians, and since $Q = 16$ from the previous ablation experiment, this model should already be highly discriminative. However, the effectiveness of the former deserves more careful consideration. Remember that $\Psi_l^{\text{Multi}} * \mathcal{F} = (\Psi_l * \mathcal{F}) + (\tilde{\mathbf{H}}_l * \mathcal{F})$, where \mathcal{F} can be either a decoder filter at depth l or an encoder filter at depth $(l + 1) \leq L$ (we omit MaxPooling2D here for simplicity). The output of this convolution depends linearly on Ψ_l and $\tilde{\mathbf{H}}_l$, and since $\Psi_l, \tilde{\mathbf{H}}_l \geq 0$, the sum aggregation bounds the response of this convolution. Choosing the sigmoid makes it so that $\tilde{\mathbf{H}}_l$ gates the point-wise magnitude of this convolution, similarly to an SE pathway, but in the spatial dimension. It also prevents the result of this operation from being dominated by $\tilde{\mathbf{H}}_l$.

Finally, we surmise that the effectiveness of the linear model reveals that the proposed aggregation is sensitive to the dying ReLU problem, which may negate the contribution or identification of informative level sets due to initialization of either (23) or ϕ [41]. Note that also that a general singularity spectrum is well defined for the entirety of the real numbers [21]. Architectural tweaks in this module should be further explored in future work.

5.5 Analysis of Global Channel Attention Functions

The authors of the original SE paper [22] argued, for the task of image classification, that the excitations appeared to be more class-specific as $l \rightarrow L$, becoming (at least) visually separable before the output layer (see Fig. 7). Since for segmentation each input location maps to each output, and this relationship becomes impossible to estimate given the lack of spatial resolution of the excitations g .

We use the linear estimation of the covariance of the excitations $g(\psi_l)$. We denote the covariance matrix as $\mathbf{A} \in \mathbb{R}^{C_l \times C_l}$ such that $\mathbf{A} := \frac{1}{n-1} g(\psi_l)^T g(\psi_l)$, where n is the size of a validation set. Note that this aligns with recent trends in deep learning theory that state that, under mild assumptions, deep representations tend to display linear behaviour after training [48, 24].

Since we deal only with binary tasks, we use how much information \mathbf{A}_k , the singular value decomposition of \mathbf{A} using only its top k singular values, captures about the variance of the neurons (see Fig. 7). We define the *linear excitation threshold*, $\delta \in (0, 1]$ as:

$$\operatorname{argmin}_k \frac{|\mathbf{A}_k|_F^2}{|\mathbf{A}|_F^2} \geq \delta. \quad (26)$$

Table 4: Compute requirements. Inference and train times averaged over 1000 steps using a NVIDIA GeForce RTX 3090 GPU.

| | U-Net [57] | +cSE [22] | +scSE [58] | +SRM [38] | +FCA [53] | +Mono | +Multi |
|---------------------------------|------------|-----------|------------|-----------|-----------|-----------|-----------|
| Total parameters | 1,946,881 | 1,968,721 | 1,968,948 | 1,947,783 | 3,022,417 | 1,989,105 | 1,967,553 |
| Trainable parameters | 1,946,881 | 1,968,721 | 1,968,948 | 1,947,335 | 1,968,721 | 1,969,169 | 1,947,521 |
| Non-trainable parameters | 0 | 0 | 0 | 448 | 1,053,696 | 19,936 | 20,032 |
| Train time (ms/step) | 60 | 73 | 104 | 77 | 76 | 165 | 450 |
| Inference time (ms/step) | 40 | 45 | 64 | 50 | 69 | 115 | 220 |

In simple terms, for a fixed δ , if the excitations are linearly related to the target variable, then one expects the minimum $k \rightarrow 2$.

Analysis of this surrogate task with $\delta = 0.95$, for each model and dataset pair, yielded three main insights:

(i) *There is no strong evidence of filtering of non-informative channels:* a common intuition behind channel attention functions is that they somehow learn to select only the most informative channels [58, 18, 4]. We were not able to measure such an effect in our experiments, at least for the cases when the attention modules actually increase baseline performance. For example, Monofractal recalibration displays the highest performance for the ISIC18 dataset (see Table 1), although most of the channels are not weighted aggressively by its excitations (see Fig. 8).

(ii) *The covariance of g depends monotonically on l due to its skip-connections:* we tested measuring the excitation threshold by removing the skip-connections of the U-Net (see Fig. 9, cSE-NS) and found that this would break the monotonic quasi-linear relationship between l and k . A similar behaviour was identified by the original authors of the SE [22] for classification. Since $C_0 \ll C_l$, this also suggests that the dimension of the linear manifold where the approximation of $\text{Cov}(g)$ resides increases with l , for a given δ . This is in line with current intuitions about how more “complicated features” are learned in the later stages of a CNN [74, 54].

(iii) *Balanced instance variability appears to correlate with performance:* extreme instance variability consistently led to subpar performance, as it can be observed for SRM and FCA in Fig. 8. In contrast, both cSE and Monofractal recalibration appear to be predictable, although flexible instance variability.

6 Discussion and Conclusions

We introduce two empirical priors based on Fractal Geometry: Monofractal and Multifractal recalibration. We construct them in a principled way and integrate them successfully in practice. The proposed channel attention functions significantly enhanced a U-Net’s segmentation performance, whilst simultaneously outperforming other statistical informed channel attention functions [58, 38, 53]. Insofar as we are aware, this was the first time that Multifractal analysis was leveraged completely end-to-end for semantic segmentation.

The experiments were conducted on three public medical datasets suggest that although cSE, scSE [58] and Multifractal improve the baseline for all datasets, only Multifractal recalibration does so in a statistically significant manner for all cases.

Our analysis includes other statistical priors that extend traditional SE by including higher order information in some capacity, specifically the SRM [38] and FCA [53]. Surprisingly, they generally underperformed in our experiments. In terms of global channel statistical descriptors, with the exception of the Kvasir-SEG dataset, Monofractal recalibration offers superior performance.

Our empirical analysis also reveals that global channel attention function effectiveness is potentially linked with instance variability, not to the degree to which these attention models “filter out”

some channels [22, 67, 51, 18]. On the extremes, we observed instances where instance variability was excessive (SRM) or close to 0 (FCA), and in both cases, performance decreased on average. On the other hand, both cSE and Monofractal recalibration offer balanced instance variability but have markedly different average gating responses (refer to Figure 4). We also demonstrated through experiment that, for the U-Net architecture, the excitation responses seem to get more chaotic with the depth of the encoder, which can be likely attributed to an effect of its skip connections.

We also take a more theoretically grounded approach than previous work in end-to-end (multi)fractal analysis for the context of classification tasks [72, 11, 10]. Notwithstanding, not all limitations were overcome. For instance, in order to keep computation time reasonable, we had to resort to a simple OLS estimate using a fixed small number of scales. Our recalibration modules require less compute than [72, 11, 10], yet they still take a considerable amount of extra computational time when compared to the other recalibration strategies studied in this paper (see Table 4). However, we achieve a model size that is very close to the baseline U-Net.

Our inductive prior also relies on the assumption that each filter will define a self-similar measure in order for the OLS step carried out to estimate a quantity that relates to the scaling exponents. We believe some of these problems might be overcome by further exploring the connections of CNNs with Wavelet Scattering [7] which potentially will allow to leverage more sophisticated multifractal formalisms [1, 31, 65].

References

- [1] Patrice Abry, Stéphane Jaffard, and Herwig Wendt. A bridge between geometric measure theory and signal processing: Multifractal analysis. In *Operator-Related Function Theory and Time-Frequency Analysis: The Abel Symposium 2012*, pages 1–56. Springer, 2015.
- [2] Walid Al-Dhabyani, Mohammed Gomaa, Hussien Khaled, and Aly Fahmy. Dataset of breast ultrasound images. *Data in brief*, 28:104863, 2020.
- [3] Chamidu Atupelage, Hiroshi Nagahashi, Masahiro Yamaguchi, Michiie Sakamoto, and Akinori Hashiguchi. Multifractal feature descriptor for histopathology. *Analytical Cellular Pathology*, 35(2):123–126, 2012.
- [4] Reza Azad, Ehsan Khodapanah Aghdam, Amelie Rauland, Yiwei Jia, Atlas Haddadi Avval, Afshin Bozorgpour, Sanaz Karimijafarbigloo, Joseph Paul Cohen, Ehsan Adeli, and Dorit Merhof. Medical image segmentation review: The success of u-net. *arXiv preprint arXiv:2211.14830*, 2022.
- [5] Michael F Barnsley, Robert L Devaney, Benoit B Mandelbrot, Heinz-Otto Peitgen, Dietmar Saupe, Richard F Voss, Yuval Fisher, and Michael McGuire. *The science of fractal images*, volume 1. Springer, 1988.
- [6] Phil Brodatz. Textures: a photographic album for artists and designers. (*No Title*), 1966.
- [7] Joan Bruna and Stéphane Mallat. Invariant scattering convolution networks. *IEEE transactions on pattern analysis and machine intelligence*, 35(8):1872–1886, 2013.
- [8] Saptarshi Chatterjee, Debangshu Dey, and Sugata Munshi. Optimal selection of features using wavelet fractal descriptors and automatic correlation bias reduction for classifying skin lesions. *Biomedical signal processing and control*, 40:252–262, 2018.

- [9] Bidyut Baran Chaudhuri and Nirupam Sarkar. Texture segmentation using fractal dimension. *IEEE Transactions on pattern analysis and machine intelligence*, 17(1):72–77, 1995.
- [10] Yuxuan Chen, Anze Xu, Lin Yang, Jingzhong Li, Yue Jin, and Zhen Shi. Mfen: A multi-layer fractal encoding network based on color distribution for road surface condition recognition. *IEEE Transactions on Intelligent Vehicles*, 2024.
- [11] Zhile Chen, Feng Li, Yuhui Quan, Yong Xu, and Hui Ji. Deep texture recognition via exploiting cross-layer statistical self-similarity. In *Proceedings of the IEEE/CVF conference on Computer Vision and Pattern Recognition*, pages 5231–5240, 2021.
- [12] Ashvin B Chhabra, Charles Meneveau, Roderick V Jensen, and KR Sreenivasan. Direct determination of the $f(\alpha)$ singularity spectrum and its application to fully developed turbulence. *Physical Review A*, 40(9):5284, 1989.
- [13] Noel Codella, Veronica Rotemberg, Philipp Tschandl, M Emre Celebi, Stephen Dusza, David Gutman, Brian Helba, Aadi Kalloo, Konstantinos Liopyris, Michael Marchetti, et al. Skin lesion analysis toward melanoma detection 2018: A challenge hosted by the international skin imaging collaboration (isic). *arXiv preprint arXiv:1902.03368*, 2019.
- [14] Carl JG Evertsz and Benoit B Mandelbrot. Multifractal measures. *Chaos and fractals*, 1992:921–953, 1992.
- [15] Kenneth Falconer. *Fractal geometry: mathematical foundations and applications*. John Wiley & Sons, 2004.
- [16] Zilin Gao, Jiangtao Xie, Qilong Wang, and Peihua Li. Global second-order pooling convolutional networks. In *Proceedings of the IEEE/CVF Conference on computer vision and pattern recognition*, pages 3024–3033, 2019.
- [17] Ian Goodfellow, David Warde-Farley, Mehdi Mirza, Aaron Courville, and Yoshua Bengio. Maxout networks. In *International conference on machine learning*, pages 1319–1327. PMLR, 2013.
- [18] Meng-Hao Guo, Tian-Xing Xu, Jiang-Jiang Liu, Zheng-Ning Liu, Peng-Tao Jiang, Tai-Jiang Mu, Song-Hai Zhang, Ralph R Martin, Ming-Ming Cheng, and Shi-Min Hu. Attention mechanisms in computer vision: A survey. *Computational visual media*, 8(3):331–368, 2022.
- [19] Michael Häfner, Toru Tamaki, Shinji Tanaka, Andreas Uhl, Georg Wimmer, and Shigeto Yoshida. Local fractal dimension based approaches for colonic polyp classification. *Medical image analysis*, 26(1):92–107, 2015.
- [20] Thomas C Halsey, Mogens H Jensen, Leo P Kadanoff, Itamar Procaccia, and Boris I Shraiman. Fractal measures and their singularities: The characterization of strange sets. *Physical review A*, 33(2):1141, 1986.
- [21] H George E Hentschel and Itamar Procaccia. The infinite number of generalized dimensions of fractals and strange attractors. *Physica D: Nonlinear Phenomena*, 8(3):435–444, 1983.
- [22] Jie Hu, Li Shen, and Gang Sun. Squeeze-and-excitation networks. In *Proceedings of the IEEE conference on computer vision and pattern recognition*, pages 7132–7141, 2018.

- [23] Huimin Huang, Shiao Xie, Lanfen Lin, Yutaro Iwamoto, Xianhua Han, Yen-Wei Chen, and Ruofeng Tong. Scaleformer: revisiting the transformer-based backbones from a scale-wise perspective for medical image segmentation. *arXiv preprint arXiv:2207.14552*, 2022.
- [24] Minyoung Huh, Brian Cheung, Tongzhou Wang, and Phillip Isola. The platonic representation hypothesis. *arXiv preprint arXiv:2405.07987*, 2024.
- [25] Sergey Ioffe and Christian Szegedy. Batch normalization: Accelerating deep network training by reducing internal covariate shift. In *International conference on machine learning*, pages 448–456. pmlr, 2015.
- [26] Fabian Isensee, Paul F Jaeger, Simon AA Kohl, Jens Petersen, and Klaus H Maier-Hein. nnu-net: a self-configuring method for deep learning-based biomedical image segmentation. *Nature methods*, 18(2):203–211, 2021.
- [27] Fabian Isensee, Tassilo Wald, Constantin Ulrich, Michael Baumgartner, Saikat Roy, Klaus Maier-Hein, and Paul F Jaeger. nnu-net revisited: A call for rigorous validation in 3d medical image segmentation. *arXiv preprint arXiv:2404.09556*, 2024.
- [28] Atiq Islam, Syed MS Reza, and Khan M Iftekharuddin. Multifractal texture estimation for detection and segmentation of brain tumors. *IEEE transactions on biomedical engineering*, 60(11):3204–3215, 2013.
- [29] Mihai Ivanovici and Noël Richard. Fractal dimension of color fractal images. *IEEE Transactions on Image Processing*, 20(1):227–235, 2010.
- [30] Mihai Ivanovici, Noël Richard, and Dietrich Paulus. Color image segmentation. *advanced color image processing and analysis*, pages 219–277, 2013.
- [31] Stéphane Jaffard, Stéphane Seuret, Herwig Wendt, Roberto Leonarduzzi, and Patrice Abry. Multifractal formalisms for multivariate analysis. *Proceedings of the Royal Society A*, 475(2229):20190150, 2019.
- [32] Debesh Jha, Pia H Smedsrud, Michael A Riegler, Pål Halvorsen, Thomas de Lange, Dag Johansen, and Håvard D Johansen. Kvasir-seg: A segmented polyp dataset. In *MultiMedia Modeling: 26th International Conference, MMM 2020, Daejeon, South Korea, January 5–8, 2020, Proceedings, Part II 26*, pages 451–462. Springer, 2020.
- [33] Audrey L Karperien, Herbert F Jelinek, and Helmut Ahammer. Multifractal formalism in image and time series analysis. *Brain structure and function*, 18(21):24, 2016.
- [34] Diederik Kingma and Jimmy Ba. Adam: A method for stochastic optimization. *arXiv:1412.6980*, 2014.
- [35] Redouan Korchiyne, Abderrahmane Sbihi, Sidi Mohamed Farssi, Rajae Touahni, and Mustapha Tahiri Alaoui. Medical image texture segmentation using multifractal analysis. In *2012 International Conference on Multimedia Computing and Systems*, pages 422–425. IEEE, 2012.
- [36] Alexei Kurakin. The self-organizing fractal theory as a universal discovery method: the phenomenon of life. *Theoretical Biology and Medical Modelling*, 8:1–66, 2011.

- [37] Salim Lahmiri. Glioma detection based on multi-fractal features of segmented brain mri by particle swarm optimization techniques. *Biomedical Signal Processing and Control*, 31:148–155, 2017.
- [38] HyunJae Lee, Hyo-Eun Kim, and Hyeonseob Nam. Srm: A style-based recalibration module for convolutional neural networks. In *Proceedings of the IEEE/CVF International conference on computer vision*, pages 1854–1862, 2019.
- [39] Renaud Lopes and Nacim Betrouni. Fractal and multifractal analysis: a review. *Medical image analysis*, 13(4):634–649, 2009.
- [40] Gabriele A Losa. The fractal geometry of life. In *Biology Forum/Rivista di Biologia*, volume 102, 2009.
- [41] Lu Lu, Yeonjong Shin, Yanhui Su, and George Em Karniadakis. Dying relu and initialization: Theory and numerical examples. *arXiv preprint arXiv:1903.06733*, 2019.
- [42] Jun Ma, Yuting He, Feifei Li, Lin Han, Chenyu You, and Bo Wang. Segment anything in medical images. *Nature Communications*, 15(1):654, 2024.
- [43] Miguel L. Martins, Miguel T. Coimbra, and Francesco Renna. Singularity strength recalibration of fully convolutional neural networks for biomedical image segmentation. In *Proceedings of the 2024 32nd European Signal Processing Conference (EUSIPCO)*, 2024.
- [44] Mazin Abed Mohammed, Belal Al-Khateeb, Ahmed Noori Rashid, Dheyaa Ahmed Ibrahim, Mohd Khanapi Abd Ghani, and Salama A Mostafa. Neural network and multi-fractal dimension features for breast cancer classification from ultrasound images. *Computers & Electrical Engineering*, 70:871–882, 2018.
- [45] Marcin Molski and Jerzy Konarski. Tumor growth in the space–time with temporal fractal dimension. *Chaos, Solitons & Fractals*, 36(4):811–818, 2008.
- [46] Debaleena Nawn, Sawon Pratiher, Subhankar Chattoraj, Debjani Chakraborty, Mousumi Pal, Ranjan Rashmi Paul, Srimonti Dutta, and Jyotirmoy Chatterjee. Multifractal alterations in oral sub-epithelial connective tissue during progression of pre-cancer and cancer. *IEEE Journal of Biomedical and Health Informatics*, 25(1):152–162, 2020.
- [47] Ozan Oktay, Jo Schlemper, Loic Le Folgoc, Matthew Lee, Mattias Heinrich, Kazunari Misawa, Kensaku Mori, Steven McDonagh, Nils Y Hammerla, Bernhard Kainz, et al. Attention u-net: Learning where to look for the pancreas. *arXiv preprint arXiv:1804.03999*, 2018.
- [48] Kiho Park, Yo Joong Choe, and Victor Veitch. The linear representation hypothesis and the geometry of large language models. *arXiv preprint arXiv:2311.03658*, 2023.
- [49] Maria Pedroso, Miguel L. Martins, Diogo Libânio, Mário Dinis-Ribeiro, Miguel Coimbra, and Francesco Renna. Fractal bilinear deep neural network models for gastric intestinal metaplasia detection. In *2023 IEEE EMBS International Conference on Biomedical and Health Informatics (BHI)*, pages 1–5, 2023.
- [50] Alex Pentland. Fractal-based description. In *IJCAI*, pages 973–981, 1983.
- [51] Sérgio Pereira, Adriano Pinto, Joana Amorim, Alexandrine Ribeiro, Victor Alves, and Carlos A Silva. Adaptive feature recombination and recalibration for semantic segmentation with fully convolutional networks. *IEEE transactions on medical imaging*, 38(12):2914–2925, 2019.

- [52] Anna Piantanelli, Pierluigi Maconi, Lorenzo Scalise, S Serresi, A Cialabrini, and A Basso. Fractal characterisation of boundary irregularity in skin pigmented lesions. *Medical and Biological Engineering and Computing*, 43:436–442, 2005.
- [53] Zequn Qin, Pengyi Zhang, Fei Wu, and Xi Li. Fcanet: Frequency channel attention networks. In *Proceedings of the IEEE/CVF international conference on computer vision*, pages 783–792, 2021.
- [54] Maithra Raghu, Justin Gilmer, Jason Yosinski, and Jascha Sohl-Dickstein. Svcca: Singular vector canonical correlation analysis for deep learning dynamics and interpretability. *Advances in neural information processing systems*, 30, 2017.
- [55] Anne-Marie Rickmann, Abhijit Guha Roy, Ignacio Sarasua, and Christian Wachinger. Recalibrating 3d convnets with project & excite. *IEEE transactions on medical imaging*, 39(7):2461–2471, 2020.
- [56] Guilherme Freire Roberto, Alessandra Lumini, Leandro Alves Neves, and Marcelo Zanchetta do Nascimento. Fractal neural network: A new ensemble of fractal geometry and convolutional neural networks for the classification of histology images. *Expert Systems with Applications*, 166:114103, 2021.
- [57] Olaf Ronneberger, Philipp Fischer, and Thomas Brox. U-net: Convolutional networks for biomedical image segmentation. In *Medical image computing and computer-assisted intervention–MICCAI 2015: 18th international conference, Munich, Germany, October 5–9, 2015, proceedings, part III 18*, pages 234–241. Springer, 2015.
- [58] Abhijit Guha Roy, Nassir Navab, and Christian Wachinger. Recalibrating fully convolutional networks with spatial and channel “squeeze and excitation” blocks. *IEEE transactions on medical imaging*, 38(2):540–549, 2018.
- [59] Hadrien Salat, Roberto Murcio, and Elsa Arcaute. Multifractal methodology. *Physica A: Statistical Mechanics and its Applications*, 473:467–487, 2017.
- [60] Nirupam Sarkar and Bidyut Baran Chaudhuri. An efficient differential box-counting approach to compute fractal dimension of image. *IEEE Transactions on systems, man, and cybernetics*, 24(1):115–120, 1994.
- [61] Tomislav Stojić, Irini Reljin, and Branimir Reljin. Adaptation of multifractal analysis to segmentation of microcalcifications in digital mammograms. *Physica A: Statistical Mechanics and its Applications*, 367:494–508, 2006.
- [62] Manik Varma and Rahul Garg. Locally invariant fractal features for statistical texture classification. In *2007 IEEE 11th international conference on computer vision*, pages 1–8. IEEE, 2007.
- [63] Jacques Levy Vehel and Pascal Mignot. Multifractal segmentation of images. *Fractals*, 2(03):371–377, 1994.
- [64] Haonan Wang, Peng Cao, Jiaqi Wang, and Osmar R Zaiane. Uctransnet: rethinking the skip connections in u-net from a channel-wise perspective with transformer. In *Proceedings of the AAAI conference on artificial intelligence*, volume 36, pages 2441–2449, 2022.

- [65] Herwig Wendt. *Multifractal analysis and univariate and multivariate Bayesian estimation for signals and images*. PhD thesis, Institut National Polytechnique de Toulouse, 2022.
- [66] Bruce J West. *Fractal physiology and chaos in medicine*, volume 16. World Scientific, 2012.
- [67] Sanghyun Woo, Jongchan Park, Joon-Young Lee, and In So Kweon. Cbam: Convolutional block attention module. In *Proceedings of the European conference on computer vision (ECCV)*, pages 3–19, 2018.
- [68] Yuxin Wu and Kaiming He. Group normalization. In *Proceedings of the European conference on computer vision (ECCV)*, pages 3–19, 2018.
- [69] Yong Xia, Dagan Feng, and Rongchun Zhao. Morphology-based multifractal estimation for texture segmentation. *IEEE Transactions on Image Processing*, 15(3):614–623, 2006.
- [70] Gang Xiong, Ziqin Xiong, Liqiong Jia, and Trieu-Kien Truong. Spatial multifractal spectrum distribution method for breast ultrasonic image classification. *Chaos, Solitons & Fractals*, 172:113530, 2023.
- [71] Yong Xu, Hui Ji, and Cornelia Fermüller. Viewpoint invariant texture description using fractal analysis. *International Journal of Computer Vision*, 83(1):85–100, 2009.
- [72] Yong Xu, Feng Li, Zhile Chen, Jinxiu Liang, and Yuhui Quan. Encoding spatial distribution of convolutional features for texture representation. *Advances in Neural Information Processing Systems*, 34:22732–22744, 2021.
- [73] Moi Hoon Yap, Eran A Edirisinghe, and Helmut E Bez. A novel algorithm for initial lesion detection in ultrasound breast images. *Journal of Applied Clinical Medical Physics*, 9(4):181–199, 2008.
- [74] Matthew D Zeiler and Rob Fergus. Visualizing and understanding convolutional networks. In *Computer Vision—ECCV 2014: 13th European Conference, Zurich, Switzerland, September 6–12, 2014, Proceedings, Part I 13*, pages 818–833. Springer, 2014.
- [75] Hang Zhang, Kristin Dana, Jianping Shi, Zhongyue Zhang, Xiaogang Wang, Amrith Tyagi, and Amit Agrawal. Context encoding for semantic segmentation. In *Proceedings of the IEEE conference on Computer Vision and Pattern Recognition*, pages 7151–7160, 2018.
- [76] Fobao Zhou and Wenkai Huang. Fractal few-shot learning. *IEEE Transactions on Neural Networks and Learning Systems*, 2023.

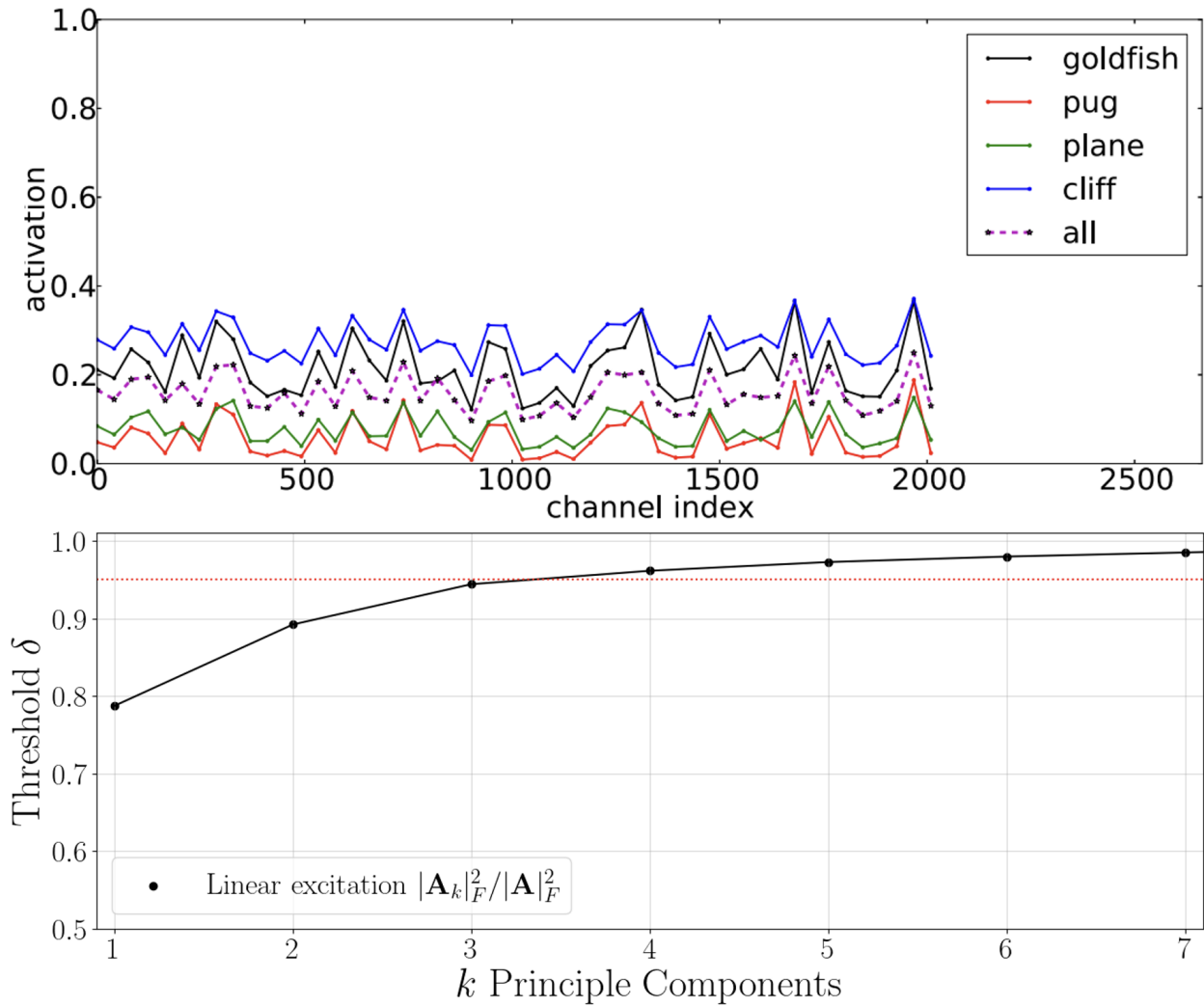


Figure 7: (Top) Excitation analysis of excitation magnitude on a ImageNet-1000 classification task, adapted from [22]. (Bottom) The number of principal components that capture $\delta = 0.95$ of the excitation variance on a binary segmentation task on the ISIC-18 dataset for the first encoder head of a U-Net deprived of its skip-connections.

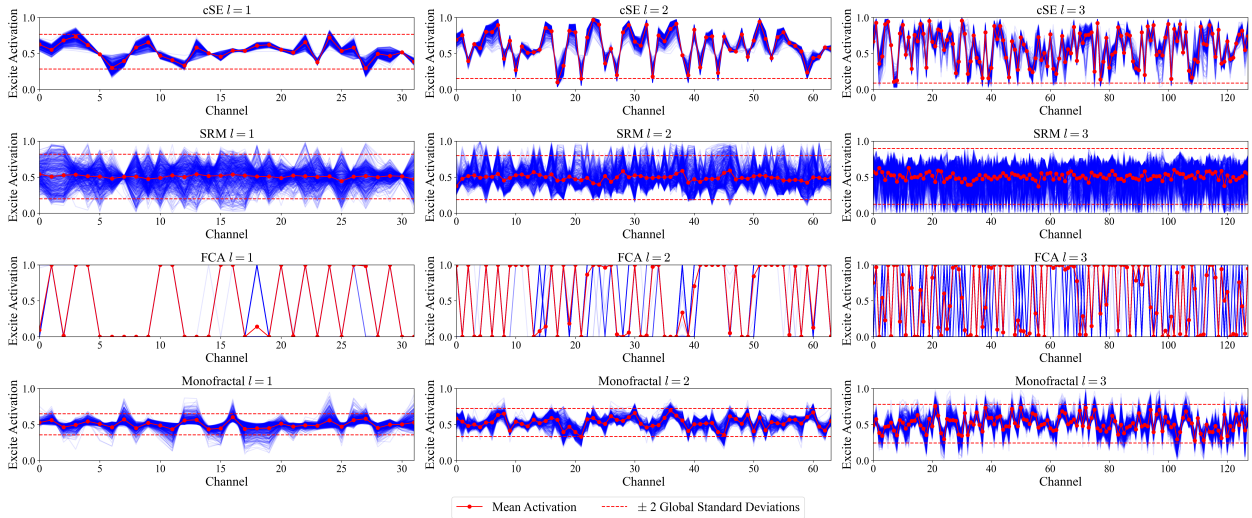


Figure 8: Test set excitation responses of cSE, SRM, FCA, and Monofractal recalibration for $l \in \{1, 2, 3\}$ in the first fold of the ISIC dataset. Each blue segment marks a response of the layer given an instance. SRM displays very heterogeneous behaviour per instance. On the opposite end of the spectrum, FCA is almost instance-agnostic. cSE and Monofractal recalibration display similar instance variability, but markedly different excitation responses around the average.

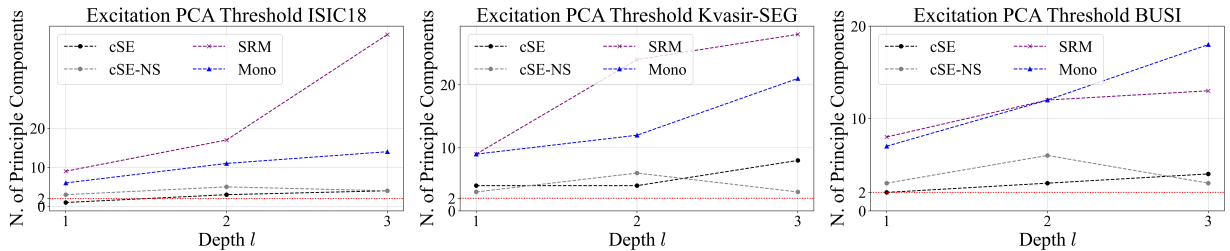


Figure 9: Number of principle components required to explain 95% of the variance for each model for every encoder depth l for each dataset. cSE-NS stands for cSE in an U-Net without skip-connections. FCA is not included due to its almost heterogeneous behavior. The U-Shape architecture makes it so that become less class-dependent as $l \rightarrow L$.